Freeze-Drying of Proteins in Glass Solids Formed by Basic Amino Acids and Dicarboxylic Acids

Ken-ichi IZUTSU,*[,a] Saori KADOYA,[b] Chikako YOMOTA,[a] Toru KAWANISHI,[a] Etsuo YONEMOCHI,[b] and Katsuhide TERADA[b]

[a] *National Institute of Health Sciences; 1–18–1 Kamiyoga, Setagaya, Tokyo 158–8501, Japan: and* [b] *Faculty of Pharmaceutical Sciences, Toho University; 2–2–1 Miyama, Funabashi, Chiba 274–8510, Japan.*
Received August 1, 2008; accepted October 11, 2008; published online October 15, 2008

The purpose of this study was to produce and characterize glass-state amorphous solids containing amino acids and organic acids that protect co-lyophilized proteins. Thermal analysis of frozen solutions containing a basic amino acid (*e.g.*, L-arginine, L-lysine, L-histidine) and a hydroxy di- or tricarboxylic acid (*e.g.*, citric acid, L-tartaric acid, DL-malic acid) showed glass transition of maximally freeze-concentrated solute at temperatures (T_g') significantly higher than those of the individual solute solutions. Mixing of the amino acid with some dicarboxylic acids (*e.g.*, oxalic acid) also suggested an upward shift of the transition temperature. Contrarily, combinations of the amino acid with monocarboxylic acids (*e.g.*, acetic acid) had T_g's between those of the individual solute solutions. Co-lyophilization of the basic amino acids and citric acid or L-tartaric acid resulted in amorphous solids that have glass transition temperatures (T_g) higher than the individual components. Mid- and near-infrared analysis indicated altered environment around the functional groups of the consisting molecules. Some of the glass-state excipient combinations protected an enzyme (lactate dehydrogenase, LDH) from inactivation during freeze-drying. The glass-state excipient combinations formed by hydrogen-bonding and electrostatic interaction network would be potent alternative to stabilize therapeutic proteins in freeze-dried formulations.

Key words freeze-drying; protein formulation; amorphous; stabilization; glass

Freeze-drying is a popular method of ensuring the stability of proteins that are not stable enough in aqueous solutions during the period required for storage and distribution.[1,2] Various freeze-dried protein formulations contain excipients (*e.g.*, sugars, polymers, and amino acids) that protect proteins from physical and chemical changes. Disaccharides (*e.g.*, sucrose, trehalose) are the most popular among them because they stabilize proteins both thermodynamically and kinetically in aqueous solutions and freeze-dried solids.[3—5]

The development of freeze-dried protein formulations containing amino acids is often more challenging than the development of formulations with saccharides because of the varied physical and chemical properties (*e.g.*, crystallinity, glass transition temperature) of the freeze-dried amino acids, as well as their tendency to form complexes with other ingredients.[6] Many amino acids are considered to protect proteins basically in similar mechanisms with disaccharides. They thermodynamically stabilize protein conformation in aqueous solutions and probably in frozen solutions by being preferentially excluded from the immediate surface of proteins.[7] Glass-state amorphous solids formed by freeze-drying of the disaccharides or some amino acids protect proteins from structural changes thermodynamically by substituting surrounding water molecules.[8] They also reduce chemical degradation of freeze-dried proteins kinetically by reducing the molecular mobility.[2,8] In addition, some amino acids (*e.g.*, L-arginine) also prevent protein aggregation in aqueous solutions prior to the drying process and after reconstitution.[9] Choosing appropriate counterions that form glass-state solid should be one of the key factors in designing amino acid-based amorphous freeze-dried formulations.[10,11] For example, glass transition temperatures (T_g) of freeze-dried L-histidine salts depend largely on the counterions.[12] Co-lyophilization of L-arginine and multivalent inorganic acids (*e.g.*, H_3PO_4, H_2SO_4) results in glass-state amorphous solids that protect proteins during the process and storage (*e.g.*, tissue plasminogen activator formulation, PDR 2003).[13] Some organic acid and inorganic cation combinations (*e.g.*, sodium citrates) also form high glass transition temperature amorphous solids.[14] Various functional groups (*e.g.*, amino, carboxyl, hydroxyl) in the constituting molecules contributes significantly to form the glass-state amorphous salt solids.[15] Producing glass-state amorphous solids by freeze-drying of amino acid and organic acid combinations, and their application in pharmaceutical formulations are interesting topics to explore.[15]

The purpose of this study was to produce stable amorphous solids that protect proteins by freeze-drying combinations of amino acids and organic acids. The physical properties of frozen solutions and freeze-dried solids containing the popular excipients and model chemicals were studied. The effect of the excipient combinations on the freeze-drying of lactate dehydrogenase (LDH) was also examined.

Experimental

Materials LDH (rabbit muscle) was obtained from Sigma Chemical (St. Louis, MO, U.S.A.). Succinic acid was produced by Kanto Chemical Co. (Tokyo, Japan). L-(+)-Tartaric acid, DL-malic acid, and other chemicals were of analytical grade and were purchased from Wako Pure Chemical (Osaka, Japan). The protein solutions were dialyzed against 50 mM sodium phosphate buffer (pH 7.0), and then centrifuged (1500 *g*×5 min) and filtered (0.45 μm, polyvinyliden difluoride (PVDF), Millipore) to remove insoluble aggregates before the freeze-drying study.

Freeze-Drying A pH meter (HM-60G, TOA-DKK Co., Tokyo, Japan) was used to determine the pH of the aqueous solutions at 25 °C. A freeze-drier (Freezvac 1C, Tozai-Tsusho, Tokyo, Japan) was used to lyophilize the aqueous solutions. Aliquots of aqueous solutions (250 μl) in flat-bottom glass vials (10 mm diameter) were frozen by immersion in liquid nitrogen. The solutions were freeze-dried without shelf temperature control (20 h), and then at 35 °C (8 h). Solid samples for diffuse-reflection near-infrared analysis were prepared by freeze-drying the aqueous solutions (2 ml) in glass vials (21 mm diameter).

Thermal Analysis Thermal analysis of frozen solutions and dried solids

* To whom correspondence should be addressed. e-mail: Izutsu@nihs.go.jp

was performed using a differential scanning calorimeter (DSC) (Q-10, TA Instruments, New Castle, DE, U.S.A.) and software (Universal Analysis 2000, TA Instruments). Aliquots of aqueous solutions (10 μl) in aluminum cells were cooled from room temperature at 10 °C/min, and then scanned from −70 °C at 5 °C/min. The effect of heat-treatment (annealing) on the thermal properties of the frozen solutions was studied after the initial heating scan paused at −10 °C, then the samples were maintained at this temperature for 10 min. Thermal data were acquired in the subsequent heating from −70 °C at 5 °C/min. Freeze-dried solids (1—2 mg) in hermetic aluminum cells were subjected to the thermal analysis from −20 °C at 5 °C/min under nitrogen gas flow. Melted organic acids (approx. 5 mg, 200 °C) in aluminum cells were rapidly cooled to −50 °C, and then scanned at 5 °C/min to obtain the glass transition temperatures. Glass transition temperatures were determined as the midpoint (maximum inflection) of the discontinuities in the heat flow curves.

Powder-X-Ray Diffraction (XRD) The powder X-ray diffraction patterns were measured at various temperatures by using a Rint-Altima diffractometer (Rigaku, Tokyo, Japan) with Cu$K\alpha$ radiation at 40 kV/40 mA. The samples were scanned in the area of $5°<2\theta<35°$ at an angle speed of 15°/min by heating at 2 °C/min from room temperature.

Mid- and Near-Infrared Analysis A Fourier-transform infrared spectrophotometer (MB-104, Bomen, Quebec, Canada) with a gas generator (Balston, Haverhill, MA, U.S.A.) and Grams/32 software were used to obtain mid-infrared spectra of freeze-fried solids. Approximately 0.5 mg of the solid was mixed with dried KBr powder (250 mg) and made into tablets by compression. The KBr tablets were scanned 128 times to obtain the spectra in the 400—4000 cm^{-1} region. Near-infrared spectroscopy was performed by using a Bruker MPA system with a diffuse-reflectance integrating-sphere probe (PbS detector) and OPUS software (Ettlingen, Germany). Near-infrared light was directed upward from the bottom of the glass vials containing freeze-dried solids to obtain the reflected signal over a range of 4000—12000 cm^{-1} with a resolution of 4 cm^{-1} in 128 scans. The freeze-dried solids were measured twice by rotating the sample vials between measurements.

Activity of Lactate Dehydrogenase in Freeze-Dried Solids Aqueous solutions (250 μl) containing LDH (0.05 mg/ml) and excipients were freeze-dried in flat-bottom glass vials (10 mm diameter). One of the enzyme solutions was freeze-dried at a higher sodium phosphate buffer concentration (50 mM, pH 7.0). Other enzyme solutions contained the added excipients and lower concentration buffer components (<1 mM) diluted from the dialyzed protein solutions. Activity of LDH was obtained spectrophotometrically at 25 °C. Each 1.0 ml of assay mixture contained 0.35 mM pyruvic acid and 0.07 mM reduced nicotinamide-adenine dinucleotide (NADH) in 50 mM sodium phosphate buffer (pH 7.5). The enzyme reaction was started by the addition of LDH solution (50 μl), and the decrease in the absorbance at 340 nm was monitored. The enzyme activity (%) relative to that before freezing was shown.

Results

Physical Property of Frozen Solutions The thermal profiles of frozen solutions containing L-histidine and citric acid at various concentration ratios (total 200 mM) are shown in Fig. 1. The single-solute frozen L-histidine solution (200 mM) showed a T_g' (glass transition temperature of maximally freeze-concentrated solute) at −33.5 °C, and an exotherm peak that suggests eutectic crystallization at around −8 °C.[12] Freeze-drying of solutions at above their T_g' often induces physical collapse because of the significantly reduced local viscosity in the freeze-concentrated phase.[1] The second scan of the 200 mM L-histidine solutions after the heat-treatment (−10 °C, 10 min) gave flat thermograms that indicate crystallized solute up to the ice melting temperature (data not shown). The citric acid solution (200 mM) had a T_g' at −55.1 °C, indicating that the solute remained amorphous in the freeze-concentrated phase surrounding ice crystals. The L-histidine crystallization peak disappeared in the presence of citric acid. The two-solute frozen solutions showed transitions (T_g's) at temperatures as high as −22.8 °C at the equal (100 mM) L-histidine and citric acid concentrations.

Figure 2 shows transition temperatures (T_g') of frozen solutions containing amino acids and organic acids at various concentration ratios. Some single-solute frozen amino acid or organic acid solutions (200 mM) had apparent T_g' transitions at −44.2 °C (L-arginine), −55.1 °C (citric acid), and

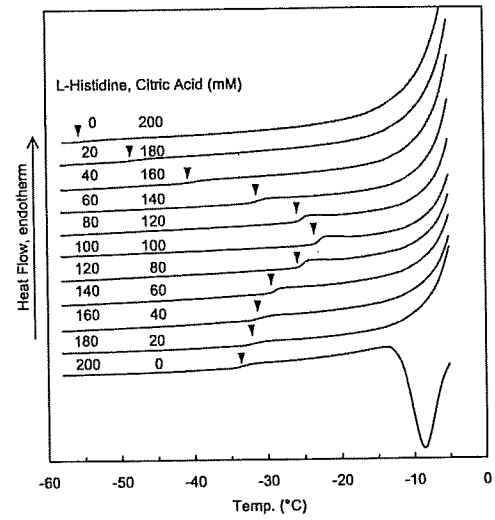

Fig. 1. Thermal Profiles of Frozen Solutions Containing L-Histidine and Citric Acid

Aliquots (10 μl) of solutions in hermetic aluminum cells were scanned from −70 °C at 5 °C/min. Glass transition temperatures of maximally freeze-concentrated solutes (T_g') are indicated by inverted triangles (▼).

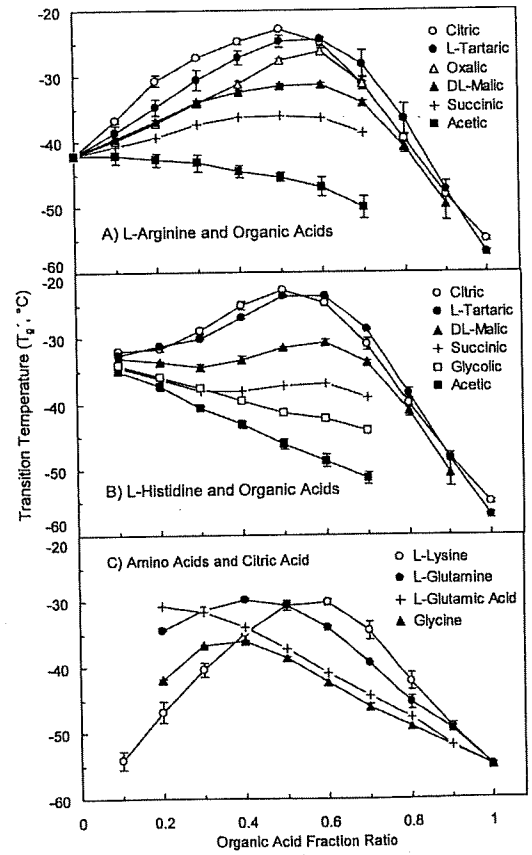

Fig. 2. Glass Transition Temperatures of Maximally Freeze-Concentrated Solute (T_g') in Frozen Solutions Containing an Amino Acid and an Organic Acid at Varied Concentration Ratios (Total 200 mM, Average±S.D., n=3)

−57.1 °C (L-tartaric acid). The frozen L-glutamine solution showed both T'_g (−42.8 °C) and the subsequent eutectic crystallization peak (approx. −25 °C) in the heating scan (data not shown). Thermograms of the frozen L-lysine and DL-malic acid solutions inclined gradually without apparent transition up to the ice melting endotherm, which suggested T'_gs lower than −60 °C. Exotherm peaks either in the cooling process (glycine, acetic acid) or in the heating scan (oxalic acid) indicated eutectic crystallization in the frozen solution.[16] Potential T'_g transitions of some frozen solutions that also showed eutectic crystallization peaks (*e.g.*, 200 mM L-histidine or L-glutamine) were not included in the figure. The limited solubility of some amino acids and organic acids (*e.g.*, L-glutamic acid, fumaric acid, maleic acid) prevented them from undergoing thermal analysis at 200 mM. A lower concentration glutamic acid solution (100 mM) showed a T'_g at −32.2 °C and an exotherm peak that suggests eutectic crystallization at around −11.0 °C (data not shown).

Mixing of the solutes induced some unique physical properties in the frozen solutions that depend on the number of functional groups in the consisting molecules. The transition temperatures (T'_gs) of frozen solutions containing a basic or neutral amino acid (L-histidine, L-arginine, L-lysine, L-glutamine, glycine) and a hydroxy di- or tricarboxylic acid (citric acid, L-tartaric acid, DL-malic acid) showed bell-shaped profiles. The frozen solutions containing a hydroxy di- or tricarboxylic acid (citric acid, L-tartaric acid) and an acidic amino acid (L-glutamic acid) did not show the mixing-induced upward T'_g shift. Citric acid also effectively prevented the crystallization of glycine in the frozen solutions. Dicarboxylic acids (succinic acid, maleic acid, fumaric acid, oxalic acid) showed a high tendency to crystallize in the single-solute frozen solutions and in some mixture frozen solutions.[15,17] The frozen solutions containing L-arginine and oxalic acid or succinic acid also presented the high transition temperature (T'_g) by mixing. A mono-carboxylic acid (acetic acid), a hydroxy mono-carboxylic acid (glycolic acid), and HCl did not show the upward T'_g shift in the mixture with the basic amino acids.[13]

Physical Property of Freeze-Dried Solids Freeze-drying of the single-solute amino acid solutions resulted in cylindrical cakes that showed varied crystallinity in the powder X-ray diffraction (XRD) and thermal analyses (Figs. 3, 4). Freeze-dried L-arginine showed the typical harrow XRD pattern of amorphous solids. Thermal scan of the solid showed the glass transition (52.6 °C) and subsequent crystallization exotherm (105—110 °C). Freeze-dried L-histidine showed largely amorphous XRD pattern (30 °C) with the broad glass transition (65—100 °C) and crystallization at varied temperatures (120—150 °C). The L-arginine and L-histidine solids showed apparent crystallization peaks in the XRD patterns at the elevated temperature (150 °C). The dried L-glutamine (200 mM) solids showed features of both crystalline (*e.g.*, peaks in the XRD pattern) and amorphous (*e.g.*, glass transitions and heat-induced crystallization exotherm) solids. The solute concentration in the initial solution and thermal history in the freeze-drying process should determine the crystallinity of the freeze-dried L-histidine and L-glutamine.[12] Glycine was freeze-dried as β polymorph crystal.[18] Freeze-drying of citric acid or L-tartaric acid solutions (200 mM) resulted in unstructured or particulate solids that

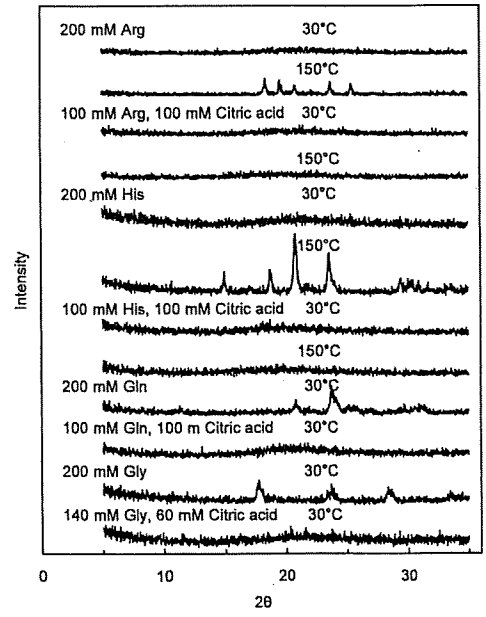

Fig. 3. Powder X-Ray Diffraction Patterns of Freeze-Dried Solids Containing Amino Acids and Citric Acid

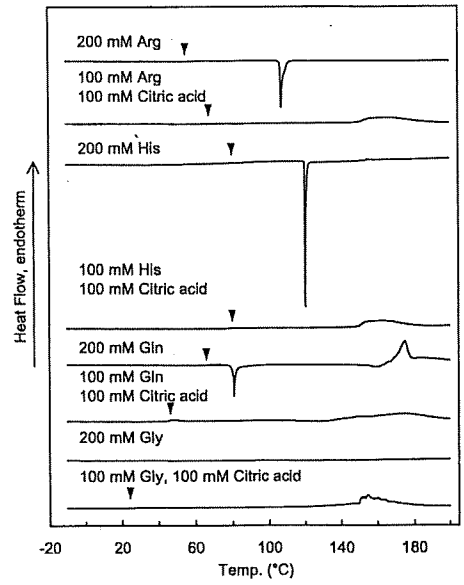

Fig. 4. DSC Thermograms of Freeze-Dried Solids Containing Amino Acids and Citric Acid

Freeze-dried solids (1—2 mg) in hermetic aluminum cells were scanned from −20 °C at 5 °C/min.

indicate physical collapse in the primary during process. Amorphous solids of the organic acids prepared by rapid-cooling of the melt liquid showed glass transition at 9.2 °C (citric acid) and 68.1 °C (L-tartaric acid) in the thermal scan (n=3).[19]

Co-lyophilizing the basic or neutral amino acids (L-arginine, L-histidine, L-glutamine, glycine) and the organic acid (citric acid, L-tartaric acid) produced cylindrical non-crystalline cake solids at wide initial concentration ratios (Figs. 3—5). The solids obtained by freeze-drying the basic amino acids (L-arginine, L-histidine) with citric or L-tartaric acid showed glass transition at temperatures (T_gs) much higher

than those of the individual components. The transitions were observed at temperatures as high as 89.5 °C (140 mM L-arginine, 60 mM citric acid) or 98.5 °C (160 mM L-histidine, 40 mM citric acid). Shrinking of some solids containing higher ratio of organic acid during the freeze-drying process suggested their low glass transition temperatures. The XRD and thermal analysis also indicated that the co-lyophilized solids remained amorphous up to 150 °C. Some binary freeze-dried solids showed a broad endotherm that suggests component decomposition at the elevated temperatures. The mixing of L-arginine with citric acid and with L-tartaric acid showed similar T_g profiles, in spite of the large difference in their transition temperatures of the cooled-melt solids. The bell-shaped profiles of the transition temperatures were significantly different from the reported transitions of binary nonionic molecule systems that follow Gordon–Taylor equation.[20] Glass transition temperatures of amorphous solids containing ideally mixed nonionic molecules without particular attractive or repulsive interactions shift between those of the individual components. Contrarily, the glass transition temperatures of co-lyophilized L-glutamine and citric acid combination solids shifted linearly between those of the individual components, which suggested absence of the particular attractive interactions between the heterogeneous molecules in the solids. Co-lyophilization of glycine and citric acid resulted in amorphous cake solids only at limited molar ratios.

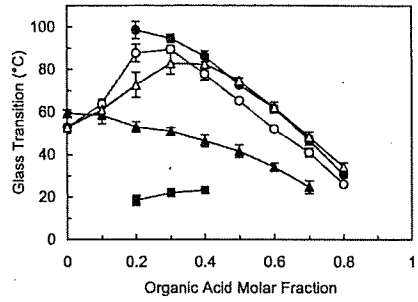

Fig. 5. Glass Transition Temperatures of Freeze-Dried Binary Solids

Each symbol denotes transition of solids containing L-arginine and citric acid (○), L-arginine and tartaric acid (△), L-histidine and citric acid (●), L-glutamine and citric acid (▲), or glycine and citric acid (■) (total: 200 mM, average±S.D., n=3).

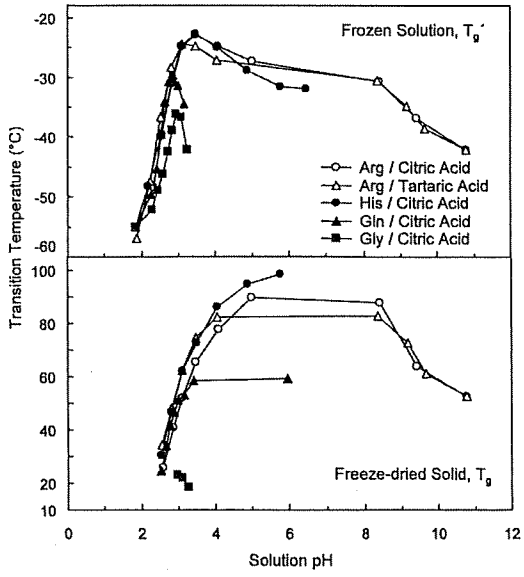

Fig. 6. Effect of Initial Solution pH (25 °C) on the Transition Temperatures of Frozen Solutions (T_g') and Freeze-Dried Solids (T_g) Containing an Amino Acid and an Organic Acid at a Fixed (0.1) Molar Concentration Ratio Intervals (200 mM Total, n=3)

Transition temperatures (T_g', T_g) of the excipient combinations obtained at a fixed (0.1) molar ratio interval were plotted against the pH of the initial solutions (25 °C, Fig. 6). Some mixtures (*e.g.*, L-arginine and citric acid, L-histidine and citric acid) yielded high T_g' frozen solutions and high T_g freeze-dried solids from weakly acidic initial solutions ($-35\,°C<T_g'$, $80\,°C<T_g$, pH 4—6), which are preferable in parenteral protein formulations. Small changes in the L-arginine and organic acid compositions (0.1 molar fraction) significantly shifted pH at the neutral region.

The mid- and near-infrared spectra of the freeze-dried L-arginine and citric acid combinations showed broad absorption bands that are typical of amorphous solids (Figs. 7, 8).[21] Co-lyophilization with citric acid reduced an amino group absorption band of L-arginine at 1550 cm^{-1} in the mid-IR spectra (KBr method), indicating altered environment of the functional group. Similar reduction of the amino group band has been reported in L-arginine–HCl salt crystal and L-argi-

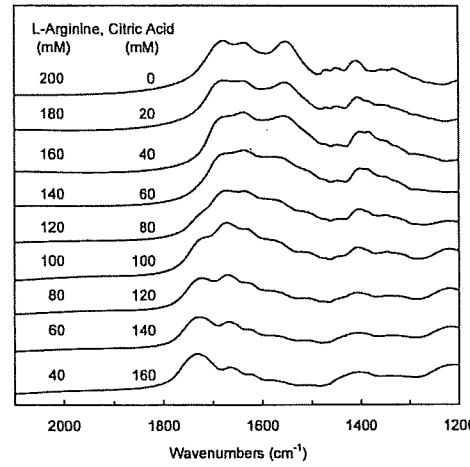

Fig. 7. Mid-Infrared Spectra of Freeze-Dried L-Arginine and Citric Acid Combinations Obtained by a KBr Tablet Method (128 Scans)

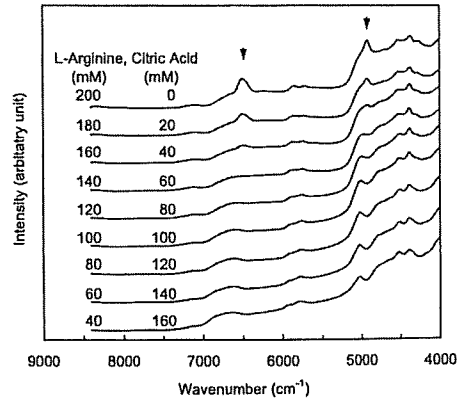

Fig. 8. Diffuse-Reflection Near-Infrared Spectra of Freeze-Dried L-Arginine and Citric Acid Combinations Obtained at the Bottom of the Glass Vials (128 Scans)

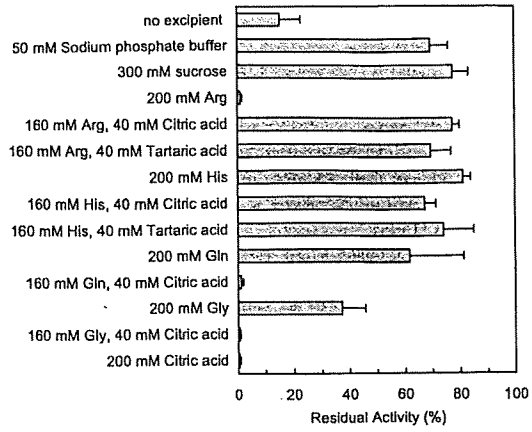

Fig. 9. Effect of Amino Acid and Organic Acid Combinations on the Activity of Freeze-Dried Lactate Dehydrogenase (50 μg/ml, Average±S.D., n=3)

nine freeze-dried with inorganic acids (*e.g.*, HCl, H_3PO_4).[13] A carboxyl group band at 1725 cm^{-1} appeared when the citric acid ratio was increased. Diffuse-reflection near-infrared spectra obtained non-destructively at the bottom of the glass vials also indicated the altered local environment of the functional groups. A large amino band of L-arginine (6505 cm^{-1}, N–H stretching 1st overtone) disappeared in the presence of lower molar concentration ratio of citric acid in the initial solution (140 mM L-arginine, 60 mM citric acid). Increasing the citric acid ratio also reduced the large absorption band at 4920 cm^{-1}, and concomitantly induced band at 5030 cm^{-1} in the co-lyophilized solids. Assignment of these bands remains to be elucidated. The results strongly suggested hydrogen-bonding and/or electrostatic interactions between L-arginine and citric acid in the lyophilized solids.

Effect of Excipients on Inactivation of Freeze-Dried LDH Freeze-drying of LDH in the absence of the stabilizing excipients resulted in significant reduction of the activity (approximately 15% of the initial solution) (Fig. 9). Higher enzyme activity was retained in freeze-drying at a higher phosphate buffer concentration (50 mM). Some amino acid and organic acid combinations that provide neutral to weakly acidic initial solution (pH 5—8) and amorphous dried solids also retained the enzyme activity. The enzyme lost most of the activity in freeze-drying from extreme pH solutions (*e.g.*, 200 mM L-arginine, pH 10.6). Addition of citric acid or L-tartaric acid slightly reduced the effect of L-histidine to retain the activity of LDH during freeze-drying. Crystallization of glycine in the single-solute frozen solution, and concomitant loss of the protecting effect, should explain the lower remaining enzyme activity.[1,2,22]

Discussion

The freeze-drying of aqueous solutions containing some basic or neutral amino acid (*e.g.*, L-arginine, L-histidine) and hydroxy di- or tricarboxylic acid (*e.g.*, citric acid, L-tartaric acid) combinations resulted in the glass-state amorphous solid cakes that protect proteins from dehydration stresses. Some of the solids showed glass transition temperatures comparable to those of disaccharides (*e.g.*, sucrose, trehalose).[4] The data and recent literature on the properties of related substances in different physical states (*e.g.*, complex crystals, ionic liquids) strongly suggested contribution of the multiple functional groups of the consisting molecules to form the interaction (*e.g.*, electrostatic, hydrogen-bonding) networks required for the glass-state amorphous solids.[23—25] Multiple amino, carboxyl, and hydroxyl groups in the solute molecules raise transition temperatures of the mixture frozen solutions (T_g') and the freeze-dried solids (T_g).[15] The ammonium carbohydrate ion pairs form multiple hydrogen-bondings in some non-polar solvents.[23,24] Differently protonated carboxyl and carboxylate groups also form an intermolecular hydrogen-bonding network.[25]

The amino acids and organic acids containing plural amino or carboxyl groups should have large chance to form the interactions with multiple counterpart molecules. The contribution of the multiple functional groups should explain the high transition temperatures (T_g', T_g) of the L-arginine and citric acid combination. L-Arginine also forms stable amorphous freeze-dried solids with multivalent inorganic acids (*e.g.*, H_3PO_4).[11,13] Frozen sodium citrate and tartrate buffer solutions exhibit the highest T_g' at certain sodium concentration ratios.[17] Supramolecular interactions (*e.g.*, peptide-like periodic interactions) reported in some complex crystals of amino acid and dicarboxylic acid (*e.g.*, L-arginine and adipic acid, X-ray analysis)[26] should support the possible multi-molecular interaction network in the less-ordered amorphous phase.

Hydroxyl groups in the citric acid, L-tartaric acid, and DL-malic acid should introduce additional hydrogen bonding to the amorphous phase. The number of hydroxyl groups in the component, and the accompanying change in the molecular interactions are major factors in determining the glass transition temperature of some ionic liquids composed of an amino acid and a 1-allylimidazolium cation.[27] The intense interactions and resulting reduction of the molecular mobility may prevent the crystallization of amino acids (*e.g.*, glycine, glutamine) at concentration ratios much lower than those of "inert" nonionic solutes (*e.g.*, sucrose) or inorganic salts (*e.g.*, NaCl).[17,30—32]

The high glass transition temperature amorphous solids formed by combinations of popular excipients would be a practical alternative to disaccharides in the design of freeze-dried protein formulations. The excipient combinations would satisfy the two major protein-stabilizing mechanisms postulated on saccharides, namely substitution of the surrounding water molecules by hydrogen-bonding and reduction of the chemical reaction by embedding in the glass-state solids.[6—8] Additional effects of some amino acids (*e.g.*, reduced aggregation in aqueous solution by L-arginine) preferable in protein formulations are also anticipated.[9] The limited crystallinity and low volatility of the amino acid and organic acid should reduce the risk of pH change and the resulting protein inactivation in the freeze-drying process reported in some buffer systems.[28]

Various proteins degrade during the freeze-drying process and subsequent storage through several chemical and physical mechanisms.[3,29] The low concentration LDH solution is often used as a model system for studying the effect of co-solutes in the freeze-thawing and freeze-drying processes because of its apparent tendency to lose its activity due to irreversible subunit dissociation and conformation change.[30] The ability of excipient combinations to retain the enzyme

activity in the freeze-drying process should indicate the stabilization of the quarterly structure against freeze-concentration and dehydration stress. Different molecular mobility, local pH, water content, and crystallinity of the excipients may affect the chemical degradation rate of the freeze-dried enzyme in the subsequent storage. The freeze-dried basic amino acid and organic acid combination solids should provide the embedded proteins with unique local environments that are significantly different from those of the nonionic excipients (*e.g.*, saccharides). The structural and chemical stability of proteins in these solids during the freeze-drying process and storage is an intriguing topic that needs further study through various model protein and stress systems.

References

1) Nail S. L., Jiang S., Chongprasert S., Knopp S. A., *Pharm. Biotechnol.*, **14**, 281—360 (2002).
2) Tang X., Pikal M. J., *Pharm. Res.*, **21**, 191—200 (2004).
3) Carpenter J. F., Arakawa T., Crowe J. H., *Dev. Biol. Stand.*, **74**, 225—238 (1992).
4) Franks F., *Dev. Biol. Stand.*, **74**, 9—18 (1992).
5) Lee J. C., Timasheff S. N., *J. Biol. Chem.*, **256**, 7139—7201 (1981).
6) Chang B. S., Randall C., *Cryobiology*, **29**, 632—656 (1992).
7) Arakawa T., Timasheff S. N., *Arch. Biochem. Biophys.*, **224**, 169—177 (1983).
8) Sane S. U., Wong R., Hsu C. C., *J. Pharm. Sci.*, **93**, 1005—1018 (2004).
9) Tsumoto K., Umetsu M., Kumagai I., Ejima D., Philo J. S., Arakawa T., *Biotechnol. Prog.*, **20**, 1301—1308 (2004).
10) Osterberg T., Fatouros A., Mikaelsson M., *Pharm. Res.*, **14**, 892—898 (1997).
11) Mattern M., Winter G., Kohnert U., Lee G., *Pharm. Dev. Technol.*, **4**, 199—208 (1999).
12) Osterberg T., Wadsten T., *Eur. J. Pharm. Sci.*, **8**, 301—308 (1999).
13) Izutsu K., Fujimaki Y., Kuwabara A., Aoyagi N., *Int. J. Pharm.*, **301**, 161—169 (2005).
14) Li J., Chatterjee K., Medek A., Shalaev E., Zografi G., *J. Pharm. Sci.*, **93**, 697—712 (2004).
15) Kadoya S., Izutsu K., Yonemochi E., Terada K., Yomota C., Kawanishi T., *Chem. Pharm. Bull.*, **56**, 821—826 (2008).
16) Akers M. J., Milton N., Byrn S. R., Nail S. L., *Pharm. Res.*, **12**, 1457—1461 (1995).
17) Shalaev E. Y., Johnson-Elton T. D., Chang L., Pikal M. J., *Pharm. Res.*, **19**, 195—201 (2002).
18) Chongprasert S., Knopp S. A., Nail S. L., *J. Pharm. Sci.*, **90**, 1720—1728 (2001).
19) Lu Q., Zografi G., *J. Pharm. Sci.*, **86**, 1374—1378 (1997).
20) Shamblin S. L., Taylor L. S., Zografi G., *J. Pharm. Sci.*, **87**, 694—701 (1998).
21) Yonemochi E., Inoue Y., Buckton G., Moffat A., Oguchi T., Yamamoto K., *Pharm. Res.*, **16**, 835—840 (1999).
22) Anchordoquy T. J., Carpenter J. F., *Arch. Biochem. Biophys.*, **332**, 231—238 (1996).
23) Sada K., Tani T., Shinkai S., *Synlett*, **2006**, 2364—2374 (2006).
24) Yerger E. A., Barrow G. M., *J. Am. Chem. Soc.*, **77**, 6206—6207 (1955).
25) Kobayashi N., Naito T., Inabe T., *Bull. Chem. Soc. Jpn.*, **76**, 1351—1362 (2003).
26) Roy S., Singh D. D., Vijayan M., *Acta Crystallogr. B*, **61**, 89—95 (2005).
27) Fukumoto K., Yoshizawa M., Ohno H., *J. Am. Chem. Soc.*, **127**, 2398—2399 (2005).
28) Li J., Guo Y., Zografi G., *Pharm. Res.*, **19**, 20—26 (2002).
29) Manning M. C., Patel K., Borchardt R. T., *Pharm. Res.*, **6**, 903—918 (1989).
30) Seguro K., Tamiya T., Tsuchiya T., Matsumoto J. J., *Cryobiology*, **27**, 70—79 (1990).

Feasibility of ^{19}F-NMR for Assessing the Molecular Mobility of Flufenamic Acid in Solid Dispersions

Yukio Aso,* Sumie Yoshioka, Tamaki Miyazaki, and Toru Kawanishi

National Institute of Health Sciences; 1–18–1 Kamiyoga, Setagaya, Tokyo 158–8501, Japan.
Received September 9, 2008; accepted October 22, 2008; published online October 23, 2008

The purpose of the present study was to clarify the feasibility of ^{19}F-NMR for assessing the molecular mobility of flufenamic acid (FLF) in solid dispersions. Amorphous solid dispersions of FLF containing poly(vinylpyrrolidone) (PVP) or hydroxypropylmethylcellulose (HPMC) were prepared by melting and rapid cooling. Spin–lattice relaxation times (T_1 and $T_{1\rho}$) of FLF fluorine atoms in the solid dispersions were determined at various temperatures (−20 to 150 °C). Correlation time (τ_c), which is a measure of rotational molecular mobility, was calculated from the observed T_1 or $T_{1\rho}$ value and that of the T_1 or $T_{1\rho}$ minimum, assuming that the relaxation mechanism of spin–lattice relaxation of FLF fluorine atoms does not change with temperature. The τ_c value for solid dispersions containing 20% PVP was 2—3 times longer than that for solid dispersions containing 20% HPMC at 50 °C, indicating that the molecular mobility of FLF in solid dispersions containing 20% PVP was lower than that in solid dispersions containing 20% HPMC. The amount of amorphous FLF remaining in the solid dispersions stored at 60 °C was successfully estimated by analyzing the solid echo signals of FLF fluorine atoms, and it was possible to follow the overall crystallization of amorphous FLF in the solid dispersions. The solid dispersion containing 20% PVP was more stable than that containing 20% HPMC. The difference in stability between solid dispersions containing PVP and HPMC is considered due to the difference in molecular mobility as determined by τ_c. The molecular mobility determined by ^{19}F-NMR seems to be a useful measure for assessing the stability of drugs containing fluorine atoms in amorphous solid dispersions.

Key words ^{19}F-NMR; molecular mobility; stability; crystallization; solid dispersion

Amorphous solid dispersions are used for improving the dissolution rate and solubility of poorly soluble drugs. However, drugs in amorphous form are generally less stable than crystalline drugs because of their higher energy state and higher molecular mobility. It is well known that polymeric excipients can reduce the crystallization rate of many amorphous drugs.[1—12] This stabilization by poly(vinylpyrrolidone) (PVP) is partly attributable to its ability to decrease molecular mobility, as indicated by increases in the glass transition temperature (T_g).[9] Therefore, it is of great interest to estimate the molecular mobility of drugs in solid dispersions. Although ^{13}C-NMR relaxation measurements are useful for assessing the molecular mobility of drugs in solid dispersions,[13] the low sensitivity of ^{13}C because of its low natural abundance is a drawback of ^{13}C-NMR. In contrast to ^{13}C, ^{19}F has very favorable sensitivity in NMR experiments, since it is present in 100% natural abundance, is second only to the proton in its resonance frequency (except ^{3}H) and has a spin quantum number of 1/2. The receptivity for ^{19}F is 83% of that for ^{1}H and 4700 times of that for ^{13}C.[14] Many drugs containing fluorine atoms are listed in The Japanese Pharmacopoeia. In contrast, almost all pharmaceutical excipients do not contain fluorine atoms. ^{19}F-NMR may therefore have an advantage over ^{13}C-NMR or ^{1}H-NMR for selectivity and sensitivity when assessing the molecular mobility of drugs containing fluorine atoms in pharmaceutical dosage forms such as solid dispersions.

The orientations and molecular mobility of flufenamic acid (FLF)[15] and ^{19}F-labeled α-tocopherol[16] in a lipid bilayer were studied using ^{19}F-NMR. Structures and molecular mobility of ^{19}F-labeled peptides and proteins in biological membranes were also investigated.[17—20] To the authors' knowledge, application of ^{19}F-NMR to studies of drug molecular mobility in solid dispersions has not been reported. This paper describes the feasibility of ^{19}F-NMR for assessing the molecular mobility of FLF in PVP or hydroxypropylmethylcellulose (HPMC) solid dispersions, and discusses the effect of polymer excipients on the crystallization tendency of FLF in solid dispersions in terms of differences in molecular mobility.

Experimental

Materials FLF (Fig. 1) was purchased from Wako Pure Chemical Industry (Osaka), and PVP and HPMC were from Sigma (St. Louis, MO, U.S.A.). FLF solid dispersions with PVP or HPMC were prepared by melting and cooling of mixtures of FLF with PVP or HPMC. The solid dispersions obtained were confirmed to be amorphous from microscopic observation under polarized light.

Nuclear Magnetic Relaxation Measurements ^{19}F-NMR measurements were carried out using a model JNM-MU25 pulsed NMR spectrometer (JEOL DATUM, Tokyo) operating at a resonance frequency of 25 MHz. Time profiles of spin–spin relaxation of the ^{19}F atoms of FLF were measured using the "solid echo" pulse sequence to overcome the dead time of the instrument. Spin–lattice relaxation time in the laboratory frame (T_1) was measured using the inversion recovery pulse sequence. Spin–lattice relaxation time in the rotating flame ($T_{1\rho}$) was measured at spin locking intensity of 10 G.

DSC Measurements T_g of FLF-PVP and FLF-HPMC solid dispersions was measured by DSC using a model 2920 differential scanning calorimeter and a refrigerator cooling system (TA Instruments, Newcastle, DE, U.S.A.). Approximately 5 mg of each solid dispersions was put into an aluminum sample pan and then sealed hermetically. T_g was measured at a heating rate of 20 °C/min. Temperature calibration of the instrument was carried out using indium.

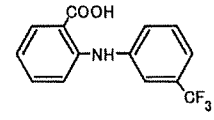

Fig. 1. Structure of FLF

* To whom correspondence should be addressed. e-mail: aso@nihs.go.jp

Results and Discussion

Molecular Mobility of FLF as Measured by ^{19}F-NMR Spin–Lattice Relaxation Time T_1 and $T_{1\rho}$ of fluorine atoms of FLF in PVP and HPMC solid dispersions were measured using a pulsed NMR spectrometer in the temperature range from −20 to 150 °C. T_1 is sensitive to the molecular motion on the time scale of the resonance frequency (MHz order). On the other hand, $T_{1\rho}$ is sensitive to the molecular motion with a frequency equivalent to the intensity of spin locking field (typically mid kHz order).[21] The temperature dependence of T_1 and $T_{1\rho}$ exhibits minimum at a specific temperature at which the molecules of interest have molecular motion with MHz time scale or mid kHz time scale predominantly. The resonance frequency of 25 MHz, lower than that of a conventional high resolution NMR spectrometer, was used to observe T_1 minimum in the temperature rage studied. Figure 2 shows the temperature dependence of T_1 and $T_{1\rho}$ of FLF fluorine atoms in PVP and HPMC solid dispersions. For FLF–PVP solid dispersions (7 : 3), the minimum of T_1 or $T_{1\rho}$ was observed at about 90 °C and 60 °C, respectively (Fig. 2A). When the PVP content decreased to 20% (w/w), T_1 and $T_{1\rho}$ of FLF at temperatures above 70 °C could not be determined due to rapid crystallization. Similar temperature dependence of T_1 or $T_{1\rho}$ was observed for the FLF–HPMC solid dispersions (Fig. 2B). The temperature difference between T_1 and $T_{1\rho}$ minimum is considered to be due to the difference in the time scale of molecular motion reflected on T_1 (MHz order) and $T_{1\rho}$ (mid kHz order). Since the molecular motion on MHz time scale becomes predominant at higher temperature than molecular motion on mid kHz time scale, T_1 minimum is observed at higher temperature than $T_{1\rho}$ minimum.

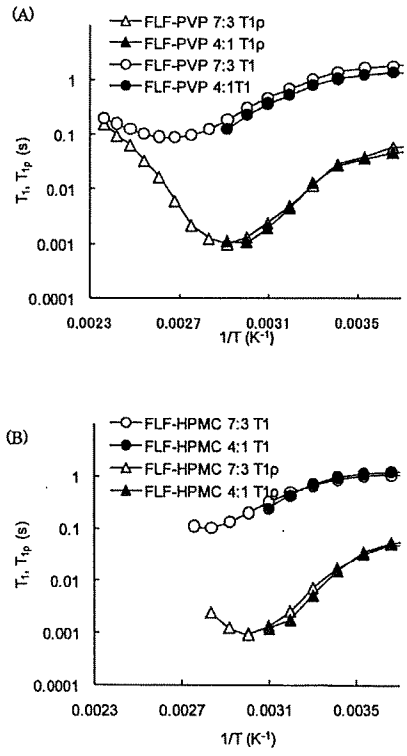

Fig. 2. Temperature Dependence of T_1 and $T_{1\rho}$ of FLF Fluorine Atoms in PVP (A) and HPMC (B) Solid Dispersions

We made following assumptions in order to estimate the molecular mobility of FLF from T_1 and $T_{1\rho}$ of FLF fluorine atoms: first, we assumed that FLF fluorine atoms in the solid dispersions relaxes mainly *via* dipolar interaction, and that the contribution of the spin–rotation interaction mechanism[21] is negligible. While relaxation *via* the spin–rotation interaction mechanism has been reported for liquid sample,[22–24] complete domination of dipolar interactions has been reported for fluorine atoms for polycrystalline van der Waals molecular solid.[25] We also made an assumption that the contribution of the cross-relaxation between fluorine and proton atoms can be considered small. It is known that relaxation is not intrinsically single-exponential when cross-relaxation between fluorine and proton atoms takes place.[14] However, we assumed small contribution of the cross-relaxation, because the relaxation of FLF fluorine atoms in the solid dispersions was exponential within experimental uncertainty. In studies of molecular motions, a large number of models describing molecular motions have been proposed for calculation of the spectrum density function.[26] We used a simple model that the molecular motion reflected on T_1 or $T_{1\rho}$ is represented by single correlation time for the purpose of comparing the mobility of FLF in the PVP and HPMC solid dispersions. According to the above assumptions, T_1 and $T_{1\rho}$ are described by Eqs. 1 and 2.[21]

$$\frac{1}{T_1} = \frac{6}{20}\frac{\gamma^4\hbar^2}{r^6}\left\{\frac{\tau_c}{1+\omega_0^2\tau_c^2} + \frac{4\tau_c}{1+4\omega_0^2\tau_c^2}\right\} \quad (1)$$

$$\frac{1}{T_{1\rho}} = \frac{3}{20}\frac{\gamma^4\hbar^2}{r^6}\left\{\frac{3\tau_c}{1+4\omega_1^2\tau_c^2} + \frac{5\tau_c}{1+\omega_0^2\tau_c^2} + \frac{2\tau_c}{1+4\omega_0^2\tau_c^2}\right\} \quad (2)$$

where τ_c is the correlation time that characterizes molecular reorientations, and ω_0 and ω_1 are the resonance frequencies of fluorine atoms in the static magnetic field and spin locking field, respectively. γ, r and $\hbar$ are the gyromagnetic ratio of fluorine, the distance of neighboring fluorine atoms, and the Plank constant divided by 2π, respectively. Equations 1 and 2 infer that T_1 and $T_{1\rho}$ become minimal when $\omega_0\tau_c$ is approximately 0.62[27] and $\omega_1\tau_c$ is approximately 0.52,[21] respectively. When the minimum of T_1 or $T_{1\rho}$ is observed, we can calculate the unknown value, r, in Eqs. 1 and 2. If r is known, the τ_c value can be calculated from the observed T_1 or $T_{1\rho}$ value, assuming that r does not change with temperature.

The values of r calculated from the T_1 and $T_{1\rho}$ minimum observed for the FLF–PVP solid dispersion (7 : 3) were 2.3 and 2.4 Å, respectively, and similar r values were obtained for the FLF–HPMC solid dispersion (7 : 3). These values are comparable to the reported value (2.174 Å) for 3-(trifluoromethyl)phenanthrene,[25] indicating that dipole interaction between neighboring fluorine atoms can be considered the predominant relaxation mechanism of FLF fluorine atoms in the solid dispersions. The difference between the r values obtained in this work and the reported value suggests that the possibility of the spin–rotation interaction mechanism and/or dipole interaction between fluorine and proton atoms cannot be excluded as a relaxation mechanism of FLF fluorine atoms.

Figure 3 shows the temperature dependence of τ_c calculated from T_1 and $T_{1\rho}$ for FLF fluorine atoms in the solid dis-

persions. The τ_c of FLF fluorine atoms in PVP solid dispersions calculated from $T_{1\rho}$ was 8.2 μs at 50 °C, which was about 3 times larger than that in HPMC solid dispersions (2.6 μs), indicating that the molecular mobility of FLF was lowered more strongly by PVP than by HPMC.

The τ_c values calculated using T_1 values differ from those calculated from $T_{1\rho}$ values. The slope of temperature dependence of τ_c changed around T_g. These findings suggest that the assumption that the molecular motion reflected on T_1 and $T_{1\rho}$ is represented by a single τ_c may be too simple to describe the molecular motion of FLF in the solid dispersions at temperatures studied, and that two or more molecular motions, such as rotation of trifluoromethyl group and motions with larger scales than rotation of trifluoromethyl group, may be reflected on T_1 and $T_{1\rho}$. Further studies including ^{1}H-NMR relaxation measurement and dielectric relaxation measurements will be needed to identify the detailed molecular motion of FLF in the solid dispersions.

Correlation between Crystallization Tendency and Molecular Mobility of FLF in Solid Dispersions Crystallization proceeds *via* formation of crystal nuclei and crystal growth. As a measure of the crystallization tendency of amorphous FLF in solid dispersions, the overall crystallization rate of amorphous FLF in the solid dispersions was estimated from the time profiles amorphous FLF remaining in the solid dispersions instead of measuring the nucleation rate and growth rate. Amorphous FLF remaining in the solid dispersions was estimated by analyzing solid echo signals of FLF fluorine atoms. Figure 4 shows the solid echo signal of fluorine atoms of FLF in solid dispersions containing 20% (w/w) PVP and that of fluorine atoms of crystalline FLF. The signal for the solid dispersions was describable by the Lorentzian relaxation equation (Eq. 3), and its relaxation time (T_{2L}) was approximately 140 μs. Crystalline FLF exhibited Gaussian relaxation signals (Eq. 4), and its relaxation time (T_{2G}) was approximately 30 μs. These results indicate that amorphous FLF in solid dispersions is considered to exhibit Lorentzian relaxation signals.

$$I=I_0 \exp(-t/T_{2L}) \tag{3}$$

$$I=I_0 \exp\{-t^2/(2T_{2G}^2)\} \tag{4}$$

where I_0 and I represent the signal intensities at time 0 and t, respectively. Figure 5 shows solid echo signals for the fluorine atoms of FLF in the solid dispersions stored at 60 °C. Samples stored at 60 °C exhibited biphasic decay signals, and signals were describable by summation of the Gaussian (solid line) and Lorentzian (dashed line) equations (Eq. 5).

$$I=I_0\{P_L \exp(-t/T_{2L})+P_G \exp(-t^2/2T_{2G}^2)\} \tag{5}$$

where P_L and P_G are the ratio of fluorine atoms exhibiting Lorentzian and Gaussian relaxation process, respectively, and $P_L+P_G=1$. Assuming that the T_{2L} and T_{2G} values are 140 and 30 μs, respectively, P_L values of FLF in the solid dispersions were estimated by curve fitting. P_L values of the solid dispersions decreased with increasing storage time, indicating that crystallization of amorphous FLF in solid dispersions takes place during storage at 60 °C. To certify the reliability of the P_L values obtained by ^{19}F-NMR measurements, change in the heat capacity at T_g ($\Delta C_p(T_g)$) was determined for the solid dispersions stored at 60 °C for various periods as a measure of amorphous FLF remaining, and was compared with the value of P_L. As shown in Fig. 6, the P_L value was proportional to the $\Delta C_p(T_g)$ value, and was considered to be a useful measure of amorphous FLF remaining in the solid dispersions.

Figure 7 shows the time profiles of the P_L values for FLF solid dispersions containing 20% (w/w) PVP or HPMC at 60 °C. The decrease in the ratio of Lorentzian fluorine atoms was faster for HPMC solid dispersions than for PVP solid dispersions, indicating that the overall crystallization rate of FLF in HPMC solid dispersions is larger than that in PVP solid dispersions. The overall crystallization rate depends on both molecular mobility (the rate of diffusion across the interface between crystalline and amorphous phase) and ther-

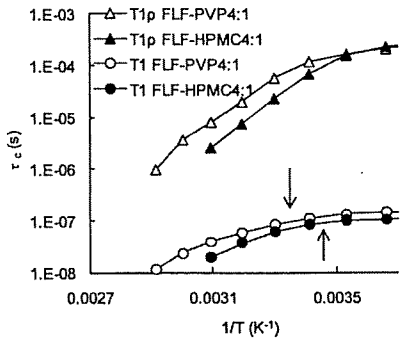

Fig. 3. Temperature Dependence of τ_c of FLF Fluorine Atoms in PVP and HPMC Solid Dispersions

Arrows in the figure represent T_g.

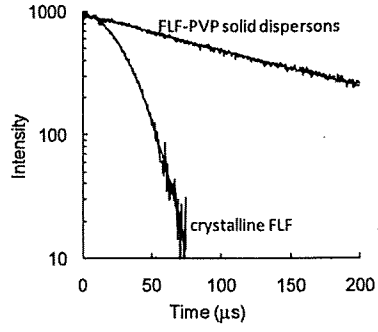

Fig. 4. Typical Solid Echo Signal of Fluorine Atoms of FLF in the Freshly Prepared Solid Dispersion Containing 20% (w/w) PVP and That of Fluorine Atoms of Crystalline FLF

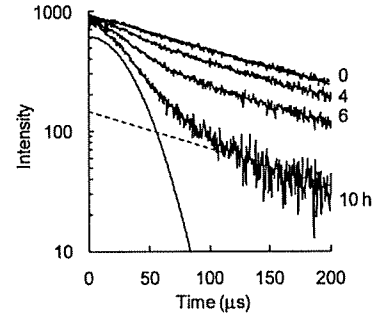

Fig. 5. Typical Solid Echo Signals of Fluorine Atoms of FLF in the Solid Dispersions Containing 20% (w/w) PVP Stored at 60 °C

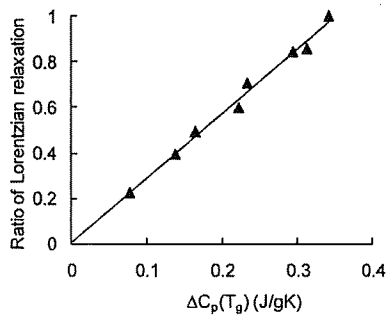

Fig. 6. The Ratio of FLF Fluorine Atoms Exhibiting Lorentzian Relaxation as a Function of Changes in the Heat Capacity at T_g

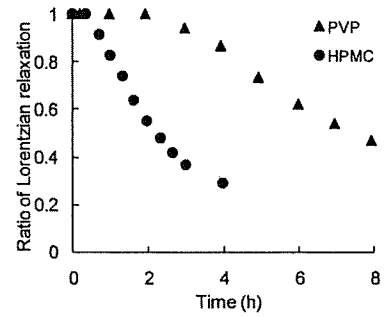

Fig. 7. Time Profiles of the Ratio of FLF Fluorine Atoms Exhibiting Lorentzian Relaxation in PVP and HPMC Solid Dispersions Stored at 60 °C

modynamic factors, such as free energy difference between crystalline and amorphous form.[2,3,10] Differences in the overall crystallization rate of amorphous FLF are consistent with those in the molecular mobility (Fig. 3), suggesting that the molecular mobility as determined by the ^{19}F-NMR spin–lattice relaxation times may be one of the factors determining crystallization rate, and useful as a measure of the physical stability of FLF in solid dispersions. The T_g values of the solid dispersions containing 20% PVP and 20% HPMC were 23 °C and 15 °C, respectively, indicating that molecular mobility reflected on T_g is higher for the solid dispersion containing HPMC than for that containing PVP. The T_g data seem to support the speculation obtained from NMR data. However, the scale of molecular mobility reflected on T_g is considered to be larger than that reflected on τ_c. Further studies should be conducted to elucidate the quantitative correlation between the physical stability of amorphous FLF and the molecular mobility determined by ^{19}F-NMR.

In conclusion, ^{19}F-NMR is useful for elucidating the molecular mobility of drugs containing fluorine atoms in amorphous solid dispersions. τ_c values of FLF fluorine atoms were calculated from the ^{19}F-NMR spin–lattice relaxation data. The τ_c value for solid dispersions containing 20% PVP was 2—3 times longer than that for solid dispersions containing 20% HPMC at 50 °C. Molecular mobility of FLF in the solid dispersions containing 20% PVP was lower than in those containing 20% HPMC, and this was consistent with the fact that the overall crystallization rate of amorphous FLF in the solid dispersion containing PVP was smaller than in that containing HPMC. The molecular mobility determined by ^{19}F-NMR seems to be useful as a measure of the physical stability of an amorphous drug in solid dispersions.

Acknowledgements Part of this work was supported by a Grant-in-aid for Research on Publicly Essential Drugs and Medical Devices from The Japan Health Sciences Foundation.

References

1) Yoshioka M., Hancock B. C., Zografi G., *J. Pharm. Sci.*, **84**, 983—986 (1995).
2) Matsumoto T., Zografi G., *Pharm. Res.*, **16**, 1722—1728 (1999).
3) Crowley K. J., Zografi G., *Pharm. Res.*, **20**, 1417—1422 (2003).
4) Shamblin S. L., Huang E. Y., Zografi G., *J. Therm. Anal.*, **47**, 1567—1579 (1996).
5) Shamblin S. L., Zografi G., *Pharm. Res.*, **16**, 1119—1124 (1999).
6) Zeng X. M., Martin G. P., Marriott C., *Int. J. Pharm.*, **218**, 63—73 (2001).
7) Miyazaki T., Yoshioka S., Aso Y., Kojima S., *J. Pharm. Sci.*, **93**, 2710—2717 (2004).
8) Khougaz K., Clas S., *J. Pharm. Sci.*, **89**, 1325—1334 (2000).
9) Berggren J., Alderborn G., *Eur. J. Pharm. Sci.*, **21**, 209—215 (2004).
10) Aso Y., Yoshioka S., Kojima S., *J. Pharm. Sci.*, **93**, 384—391 (2004).
11) Miyazaki T., Yoshioka S., Aso Y., *Chem. Pharm. Bull.*, **54**, 1207—1210 (2006).
12) Konno H., Taylor L. S., *J. Pharm. Sci.*, **95**, 2692—2705 (2006).
13) Aso Y., Yoshioka S., *J. Pharm. Sci.*, **95**, 318—325 (2006).
14) Harris R. K., Monti G. A., Holstein P., "Solid State NMR of Polymers," Chap. 6, ed. by Ando I., Asakura T., Elsevier, Amsterdam, 1998, pp. 351—414.
15) Grage S. L., Ulrich A. S., *J. Magn. Reson.*, **146**, 81—88 (2000).
16) Urano S., Matsuo M., Sakanaka T., Uemura I., Koyama M., Kumadaki I., Fukuzawa K., *Arch. Biochem. Biophys.*, **303**, 10—14 (1993).
17) Afonin S., Glaser R. W., Berditchevskaia M., Wadhwani P., Gührs K. H., Möllmann U., Perner A., Ulrich A. S., *ChemBioChem*, **4**, 1151—1163 (2003).
18) Salgado J., Grage S. L., Kondejewski L. H., Hodges R. S., McElhaney R. N., Ulrich A. S., *J. Biomol. NMR*, **21**, 191—208 (2001).
19) Williams S. P., Haggie P. M., Brindle K. M., *Biophys. J.*, **72**, 490—498 (1997).
20) Quint P., Ayala I., Busby S. A., Chalmers M. J., Griffin P. R., Rocca J., Nick H. S., Silverman D. N., *Biochemistry*, **45**, 8209—8215 (2006).
21) Farrar T. C., Brcker E. D., "Pulse and Fourier Transform NMR," Academic Press, New York and Lodon, 1971.
22) Namgoong H., Lee J. W., *Bull. Korean Chem. Soc.*, **14**, 91—95 (1993).
23) Huang S.-G., Rogers M. T., *J. Chem. Phys.*, **68**, 5601—5606 (1978).
24) Gutowsky H. S., Lawrenceson I. J., Shimomura K., *Phys. Rev. Lett.*, **6**, 349—351 (1961).
25) Beckmann P. A., Rosenberg J., Nordstrom K., Mallory C. W., Mallory F. B., *J. Phys. Chem. A*, **110**, 3947—3953 (2006).
26) Horii F., "Solid State NMR of Polymers," Chap. 3, ed. by Ando I., Asakura T., Elsevier, Amsterdam, 1998, pp. 51—82.
27) Ruan R. R., Chen P. L., "Water in Foods and Biological Materials," Chap. 7, Technomic Publishing Co., Lancaster Basel, 1998, pp. 253—278.

J Pharmacol Sci 109, 327 – 333 (2009)

Journal of Pharmacological Sciences

Forum Minireview

New Aspects for the Treatment of Cardiac Diseases Based on the Diversity of Functional Controls on Cardiac Muscles: Diversity in the Excitation–Contraction Mechanisms of the Heart

Hikaru Tanaka[1,*], Iyuki Namekata[1], Hideaki Nouchi[1], Koki Shigenobu[1], Toru Kawanishi[2], and Akira Takahara[1]

[1]*Department of Pharmacology, Toho University Faculty of Pharmaceutical Sciences, Chiba 274-8510, Japan*
[2]*Division of Drugs, National Institute of Health Science, Tokyo 158-8501, Japan*

Received October 16, 2008; Accepted November 5, 2008

Abstract. The waveform of the myocardial action potential (AP) triggering contraction differs among the species, developmental stage, and pathological state. The species difference in heart rate, which inversely correlates with body size, originates in the ion-channel mechanisms responsible for diastolic depolarization of the sinoatrial node. In some cases, such as the chronically AV-blocked dog and 11- to 13-day chick embryo, the repolarization reserve is decreased making the heart useful for drug evaluation. The degree of dependence of contraction on sarcoplasmic reticulum (SR) function increases during development. The large SR dependence and short AP of the adult mouse and rat support their rapid contraction under high heart rate. The function of the Na^+/Ca^{2+} exchanger is affected by AP waveform and ion concentrations; its major role is Ca^{2+} extrusion, but under pathological conditions such as ischemia-reperfusion, it allows Ca^{2+} influx and leads to myocardial injury, including loss of mitochondrial function. The role of mitochondria in ATP supply is less in the fetus where glycolysis plays a greater role. The pharmacological properties of the myocardium are affected by all of these factors and also by autonomic innervation and the hormonal status. Such comprehensive understanding is indispensable for the development of novel therapeutic strategies.

Keywords: heart, action potential, contraction, calcium ion, autonomic nervous system, cardiac disease

Introduction

The action potential and the Ca^{2+} transient are the common mechanisms triggering myocardial contraction, but the precise mechanisms for the generation of the action potential and Ca^{2+} handling as well as their neurohormoral regulation differs among the species, developmental stage, and pathological state. In general, the hearts of smaller animals have higher beating rates, which could be ascribed to a difference in the pacemaker depolarization mechanisms of the sinoatrial node. The time course of repolarization and Ca^{2+} transient is faster in the myocardium of smaller animals, which can be ascribed to ion-channel and Ca^{2+}-handling mechanisms. Such difference in the basic excitation–contraction mechanisms underlies the difference in pharmacological properties of the myocardium. In general, difference among species is small in the immature myocardium and become prominent towards adulthood. The pharmacological properties of the myocardium are also affected by the metabolic background and also by the presence of non-myocardial cells in the myocardium such as neurons and endocardial endothelial cells. Here we will overview the factors underlying the diversity in myocardial excitation–contraction mechanisms. For details, refer to recent reviews in each field.

*Corresponding author. htanaka@phar.toho-u.ac.jp
Published online in J-STAGE on March 7, 2009 (in advance)
doi: 10.1254/jphs.08R22FM

Pacemaker mechanisms

Cardiac pacemaking is the result of multiple ionic

mechanisms in the sinoatrial node cell (1, 2). Ion channels including the L-type calcium current (I_{CaL}), sustained inward current (I_{st}), hyperpolarization-activated inward current (I_h or I_f), T-type calcium current (I_{CaT}), and sodium calcium exchanger current (I_{NCX}) have been reported to be involved in the depolarization of the sinoatrial node action potential. The contribution of each component appears to vary among animal species. The action potential upstroke is caused by I_{CaL}, whose molecular identity was reported to include two different pore-forming subunits, Cav1.2 and Cav1.3. Most of the I_{CaL} flows through Cav1.2 in the mouse sinoatrial node while that in the porcine sinoatrial node flows exclusively through Cav1.3 (2). I_{CaT} appears to contribute to the pacemaker (phase 4) depolarization but only in smaller animals (2). Results from voltage clamp experiments as well as analysis with the selective I_{CaT} blocker $R(-)$-efonidipine (3) revealed that the I_{CaT} density in sinoatrial node cells is higher in smaller animals such as the mouse and low in larger animals such as the rabbit and pig. There is no report on the species difference of I_h and I_{st}. I_h may rather be involved in the regional variation in the maximum diastolic potential within the sinoatrial node region: the density is higher in the peripheral region of the sinoatrial node, which may function to protect the pacemaking activity at the central region from the hyperpolarizing influence of the surrounding atrial cells (1).

The rate of repolarization is determined by the density and type of potassium currents present in the sinoatrial node cells (2). The delayed rectifier potassium current I_K consists of two components, the rapidly activating I_{Kr} and the slowly activating I_{Ks}. Selective blockade of I_{Kr} by E-4031 inhibits spontaneous activity of the rabbit, guinea-pig and mouse sinoatrial node cells, and blockade of I_{Ks} by chromanol 293B inhibits those in porcine and guinea-pig sinoatrial node cells. These results suggest that the sinoatrial node automaticity is driven by I_{Kr} in smaller animals with high sinus rate and by I_{Ks} in larger animals with slower sinus rate. Some researchers postulate that pacemaking is also controlled by an intracellular clock; Ca^{2+} released from the sarcoplasmic reticulum during the diastolic period is pumped out of the cell through the forward-mode Na^+/Ca^{2+} exchanger that generates an inward current and may contribute to pacemaker depolarization (4). However, others reported that the automaticity of the sinoatrial node cells was not abolished by ryanodine, which interferes with sarcoplasmic reticulum function (5). Such discrepancy may reflect the regional variations in pacemaker mechanisms; the contribution of the intracellular clock may be larger in the peripheral region of the sinoatrial node (6). The myocardium present in the pulmonary vein, which is attracting attention as the source of ectopic automaticity responsible for the generation and maintenance of atrial fibrillation, was shown to have action potential properties different from those of the atrium (7). It shows spontaneous and ouabain-induced automaticity, which can be inhibited by either ryanodine or the Na^+/Ca^{2+} exchanger blockade. Thus, acceleration of pacemaker depolarization by the intracellular clock may be prominent in certain regions of the myocardium and/or under pathological conditions.

Action potential properties in the working myocardium

Concerning the action potential of the working myocardium, diversity is observed in the repolarization phase rather than in the depolarization phase (8). The rapid upstroke of the action potential is caused by a large I_{Na} current density that guarantees propagation of the action potential through the myocardium (9). In the adult mouse ventricular myocardium, the upstroke velocity is more than twofold higher than those observed in most other working myocardia. This might be a mechanism to compensate for the extremely short action potential duration in the adult mouse ventricle; shorter action potential duration means less electrotonic depolarizing support from behind at the activation wave front. A large diversity exists in the rate of the repolarization and the ionic currents involved among animal species and the developmental stage (ref. 8 and Fig. 1). The adult mouse ventricular myocardium has an action potential with extremely short duration at depolarized potentials of only a few ms and a late slowly repolarizing phase. Voltage clamp studies showed that the I_{Ca} density of the mouse and rat myocardium is not less than that of other species such as the guinea pig and rabbit, which has an action potential lasting as long as 200 ms. The repolarizing potassium current of the mouse and rat ventricle is the transient outward current (I_{to}), which activates much faster than I_K, the major repolarizing current of ventricular myocardia in many other animals. Thus, the diversity in repolarizing potassium currents appears to be the major cause of species difference in myocardial repolarization.

The potassium currents responsible for repolarization are influenced by the endocrine hormones and are reduced under pathological conditions and in the immature myocardium. A cardiac ion channel responsible for repolarization is known to be affected by sex hormones (10). This can at least partly explain the observed gender difference in susceptibility to the arrhythmogenic effects of QT-prolonging drugs. The hearts of the chronic AV block dog were shown to undergo structural remodeling including myocardial hypertrophy and in-

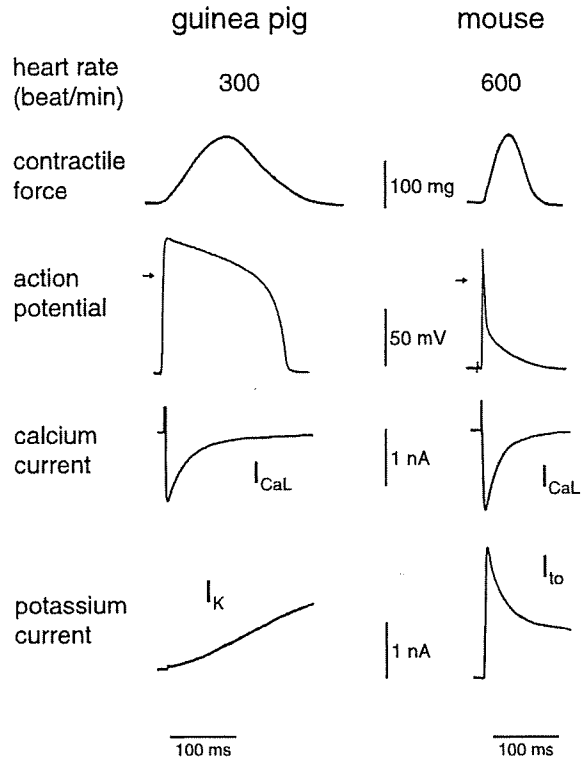

Fig. 1. Species difference in myocardial excitation–contraction properties. Typical records for the contractile force, action potential, and membrane currents of isolated myocardial tissue and cells were compared between the guinea pig and mouse.

crease in collagen fibers (11). This was accompanied by decreased expression level of potassium channels, resulting in increased action potential duration in the AV-blocked dog myocardium (12). It was also shown to have an increased sensitivity to the action potential prolonging and/or arrhythmogenic effect of drugs with potassium channel–blocking activity. Reduced repolarizing currents have been reported in immature myocardia from many animal species. In case of the guinea-pig ventricle, the densities of I_{Ca} and I_K are both decreased in the fetus compared to those in the adult (13). The fetal ventricle has an action potential with longer duration and a higher sensitivity to the prolonging effect of pharmacological agents (14). Ventricular myocardium from the 11- to 13-day chick embryo also has an increased sensitivity to action potential prolonging drugs (15). I_{Kr} blockade with E-4031 prolongs the action potential duration at this age and induces early afterdepolarization. Terfenadine, which is known for its lack of action potential–prolonging activity on isolated myocardial tissue preparations despite its QT-prolonging and arrhythmogenic activity in vivo, was shown to produce action potential prolongation in the 11- to 13-day chick embryo ventricle. Thus, myocardia from certain pathological models and from immature animals appear to have decreased repolarization reserve and may be a useful model for the investigation of arrhythmogenic mechanisms and a sensitive assay system for the action potential prolonging activity of drugs.

Ca^{2+} handling

Ventricular myocytes from the adult mammalian heart have a well-developed T-tubular system throughout the cell. During the action potential plateau, Ca^{2+} influx through the sarcolemma and T-tubules triggers Ca^{2+} release from ryanodine receptors located on the adjacent sarcoplasmic reticulum membrane. These results in a higher Ca^{2+} concentration at the Z-band region of the ventricular myocyte only for several milliseconds during the early phase of contraction, and at about 10 ms after the onset of the action potential, Ca^{2+} concentration is uniform throughout the whole cytoplasm (16). Variations exist in the relative contribution of the transsarcolemmal Ca^{2+} influx and Ca^{2+} release from the sarcoplasmic reticulum (ref. 8 and Fig. 2). The potency order for the negative inotropic effect of nicardipine, which reflects dependence on transsarcolemmal Ca^{2+} influx, was mouse < rat < guinea pig. This correlated with the species

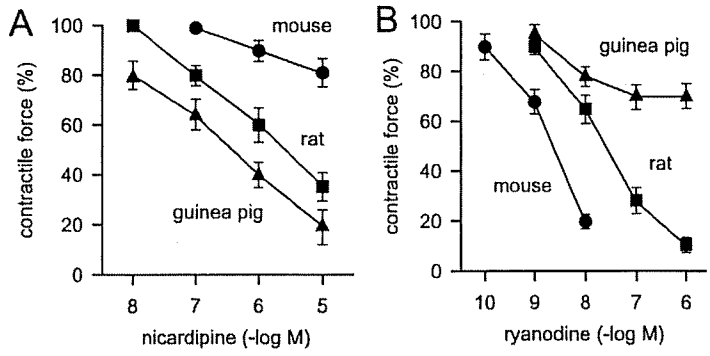

Fig. 2. Species difference in the calcium source for contraction. Negative inotropic effects of nicardipine (A), an inhibitor of transsarcolemmal Ca^{2+} influx, and ryanodine (B), an inhibitor of Ca^{2+} release from the sarcoplasmic reticulum, were compared between isolated ventricular preparations from the mouse (circles), rat (squares), and guinea pig (triangles).

difference in action potential duration. On the other hand, the potency order for the negative inotropic effects of ryanodine and cyclopiazonic acid, which reflects dependence on Ca^{2+} release from the sarcoplasmic reticulum, was mouse > rat > guinea pig. This was the same as the order of the myocardial relaxation rate. Comparative studies with various mammals revealed that hearts of smaller weight have higher resting sinus rate and higher sarcoplasmic reticulum Ca^{2+} ATPase activity. Hearts with higher beating rate require faster contraction and relaxation for sufficient refilling before the next heartbeat, which can be accomplished by increasing sarcoplasmic reticulum function. Such species difference in excitation–contraction mechanism is less prominent in immature myocardia. In the fetal myocardia, the size of the cardiomyocytes is small and the sarcoplasmic reticulum and T-tubular system are scarcely developed (17). This results in a higher dependence of contraction on transsarcolemmal Ca^{2+} influx.

In contrast to the adult ventricular myocardia where a large species difference was observed, the atrial myocardia of the mouse, rat, and guinea pig were shown to have similar high inotropic sensitivity to ryanodine, which could be explained by the atrial excitation–contraction coupling mechanisms (18). In atrial cardiomyocytes that lack a T-tubular system, transsarcolemmal Ca^{2+} influx triggers Ca^{2+} release only at the subsarcolemmal sarcoplasmic reticulum. This Ca^{2+} triggers Ca^{2+} release from the neighboring sarcoplasmic reticulum and a wave of Ca^{2+}-induced Ca^{2+} release propagates towards the cell interior. Ca^{2+} waves were more sensitive to ryanodine and cyclopiazonic acid than Ca^{2+} transients evoked by action potentials. Involvement of Ca^{2+} waves in normal atrial excitation–contraction coupling can explain the high sensitivity of atrial contraction to these agents regardless of the animal species.

Sympathetic regulation

The sympathetic nervous system is the major accelerator of myocardial function, which increases myocardial contractile force through β-adrenoceptor–mediated activation of adenylate cyclase in most animal species (19). The inotropic sensitivity to the sympathetic neurotransmitter noradrenaline is known to be affected by various factors. It is increased by hyperthyroidism and decreased under diabetic conditions. Sympathetic innervation itself exerts long-term influence on the myocardium including maintenance of its sensitivity to its own neurotransmitter. Sympathetic denervation of the heart results in supersensitivity of the myocardium not only to noradrenaline but also to other transmitters such as acetylcholine (20, 21). The fetal heart is initially devoid of sympathetic innervation. In the case of the rat, sympathetic innervation occurs at fetal day 17 at the sinoatrial node and from late embryonic period in the ventricle. The development of sympathetic innervation is followed by a tenfold decrease in the chronotropic and inotropic sensitivity of the β-adrenoceptor–mediated mechanisms (22). The time course of the functional development of the sympathetic nervous system as well as the sensitivity to autonomic transmitters are altered in pathological models such as the spontaneously hypertensive rat (23). Disturbance of the normal development of the sympathetic innervation results in alterations in responsiveness to β-adrenergic stimulation and increased susceptibility to arrhythmogenic stimuli (24). Recent studies on the roles of adenylate cyclase isoforms in the myocardium suggest that isoform-specific manipulation of the enzyme may be of value in the treatment of heart failure (25).

α-Adrenoceptors are present in the myocardium and their stimulation results in no or weak positive inotropy through mechanisms different from those of β-adrenoceptor stimulation (19). Sustained positive inotropy is observed in the rabbit, guinea pig, and rat ventricle, but in the guinea pig and rat, a transient decrease in contractile force is observed before the increase. The mouse ventricle shows a sustained negative inotropy in response to α-adrenoceptor stimulation (26) that is accompanied by decreased calcium transient amplitude (27). Electrophysiological and pharmacological analysis revealed that α-adrenoceptor stimulation activates the Na^+/Ca^{2+} exchanger and decreases the Ca^{2+} released from the sarcoplasmic reticulum (28). Interestingly, activation of the Na^+/Ca^{2+} exchanger following α-adrenoceptor stimulation was also observed in guinea-pig ventricular myocytes. The extremely short action potential of the mouse ventricular myocyte favors the Na^+/Ca^{2+} exchanger to function in the forward (Ca^{2+} extrusion) mode and decrease the Ca^{2+} transient amplitude and contractile force. In fact, in the neonatal mouse ventricle, which has an action potential of longer duration, α-aderenoceptor–mediated inotropy is positive. Similar developmental conversion of inotropy from positive to negative is observed in the mouse ventricle with endothelin I and angiotensin II (29). These results suggest that the inotropic responses of the myocardium to various active substances are largely affected by the basic excitation–contraction properties of the myocardium.

Muscarinic receptor–mediated regulation

In the ventricular myocardium, the parasympathetic neurotransmitter acetylcholine is generally considered to

show no inotropy under basal conditions and negative inotropy after elevation of adenylate cyclase activity by adrenoceptor stimulation (19). In some cases, direct negative inotropy by muscarinic receptor stimulation has been reported in ventricles from the ferret, rat, dog, and hatched chick. The negative inotropy was mediated by hyperpolarization and decrease in action potential duration in the case of the ferret, while inhibition of an intrinsically activated adenylate cyclase activity was the likely mechanism in the case of the hatched chick (30). In mammalian atria, acetylcholine is considered to produce negative inotropy through inhibition of adenylate cyclase and activation of the G-protein coupled potassium current I_{KACh}. However, there are cases in which acetylcholine induces positive inotropy. In the chick embryonic atria, acetylcholine induces positive inotropy through stimulation of M_1 receptors and activation of phosphlipase C. Muscarinic receptors are known to be present not only in cardiomyocytes but also in other cell types in the myocardium. In mouse atria, a biphasic inotropic response to acetylcholine was observed: a transient negative inotropy was followed by positive inotropy that were both inhibited with atropine (31). The positive inotropy in this case was revealed to be mediated by prostaglandins released from the endocardial endothelium (32). In other cases, muscarinic agonist–induced positive inotropy was mediated by noradrenaline released from sympathetic nerve terminals. There seems to be a large variation in the polarity and mechanism for the acetylcholine-induced inotropy, which reflects both the intrinsic properties of the cardiomyocyte and the influence of other cell types in the myocardium. Whether these mechanisms are related to the pathophysiology of the heart and the effects of therapeutic agents awaits further investigation.

Effects of ischemia

The adult myocardium has a high mitochondrial content and capacity for oxidative metabolism to produce ATP. Ischemia or hypoxia, resulting from a disruption or reduction of the coronary blood flow in vivo or its simulation in experimental systems, results in myocardial injury including Ca^{2+} overload, decreased resting membrane potential and action potential duration, loss of mitochondrial function and decreased ATP content, and marked reduction of the contractile force. Such damage is only partially recovered even if the coronary perfusion is recovered. Many agents have been reported to show protective effects against myocardial ischemia–reperfusion damage (33). In most cases, the protection appeared to be accompanied by drug-induced reduction of myocardial performance. Some agents such as Cl^--channel blockers (34) and Na^+/Ca^{2+}-exchanger inhibitors (35) showed protection against myocardial ischemia–reperfusion injury with no evidence of cardiosupression. Evidence available at present suggests that preservation of mitochondrial function is involved in the protective effect of these agents (36). Various ion channels and transporters are present on the mitochondrial membrane and their modulation has been reported to affect mitochondrial function (37). Agents that open mitochondrial K^+ channels prevents mitochondrial Ca^{2+} overload and preserves its function through partial depolarization of the mitochondrial inner membrane.

There seem to be some variations in the susceptibility to injury during ischemia and reperfusion. The hypertrophied myocardium exposed to sustained pressure- or volume-overload is known to have increased susceptibility, which may be the result of altered metabolic properties (38). Myocardial long-chain fatty acid oxidation and coupling between glycolysis and glucose oxidation are lower than normal, resulting in enhanced H^+ production in hypertrophied myocardium. Some researchers postulate that agents that alter myocardial energy metabolism through inhibition of fatty acid oxidation may be beneficial for cardioprotection against ischemic insult. The susceptibility of the myocardium to ischemic insult is also different between mature and immature myocardium. In the adult guinea-pig ventricle, experimental hypoxia results in marked shortening of the action potential duration and complete loss of contractile activity (39). In contrast, both the action potential duration and contractile force were partly maintained in the fetal ventricle. The ATP-sensitive K^+ channel, which is considered to be the primary cause of action potential shortening under hypoxic conditions, was present in similar densities in cardiomyocytes from the adult and fetus. The relative resistance to hypoxia of the fetal myocardium could rather be explained by its high dependence on glycolysis. In general, the developmental conversion of metabolism from anaerobic to aerobic appears to parallel the increase in susceptibility to ischemic insult. Thus, the most effective strategy for cardioprotection against ischemia–reperfusion may vary depending on the metabolic status of the myocardium.

Conclusion

A large diversity exists in the excitation–contraction mechanism of the myocardium that reflects diversity in the ultrastructure of the cardiomyocyte, type and amount of ion channels and various functional proteins expressed, and the metabolic status of the myocardium. These basic properties are influenced by non-cardiac cells present in the myocardium such as neurons and endocardial endo-

thelial cells, and they are altered under pathological conditions. Diversity in the chronotropic and inotropic responses to neuronal and hormonal stimuli and to various pharmacological agents can be partly explained by the underlying excitation–contraction properties. Such comprehensive understanding of the myocardium is indispensable for the extrapolation of experimental findings to the human heart and for the development of novel therapeutic strategies.

Acknowledgments

Some of the studies performed by our group was a part of the project "Research on the molecular mechanisms of appearance of age-related diseases by failure of cell function control system, and their prevention and treatment" by the "Research Center for Aging and Age related Diseases" established in the Toho University Faculty of Pharmaceutical Sciences, and was supported in part by a grant-in-aid for Research on Publicly Essential Drugs and Medical Devices to K.S. and T.K. from the Japan Health Science Foundation.

References

1 Boyett MR, Honjo H, Kodama I. The sinoatrial node, a heterogeneous pacemaker structure. Cardiovasc Res. 2000;47:658–687.
2 Ono K, Iijima T. Ionic and molecular basis of cardiac automaticity in mammalian heart. In: Mizukami Y, Ohtsuka T, editors. Molecular mechanisms of heart diseases. Trivandrum: Research SignPost; 2005. p.1–22.
3 Tanaka H, Komikado C, Namekata I, Nakamura H, Suzuki M, Tsuneoka Y, et al. Species difference in the contribution of T-type calcium current to cardiac pacemaking as revealed by *R*(–)-efonidipine. J Pharmacol Sci. 2008;107:99–102.
4 Maltsev VA, Vinogradova TM, Lakatta EG. The emergence of a general theory of the initiation and strength of the heartbeat. J Pharmacol Sci. 2006;100:338–369.
5 Honjo H, Inada S, Lancaster MK, Yamamoto M, Niwa R, Jones SA, et al. Sarcoplasmic reticulum Ca^{2+} release is not a dominating factor in sinoatrial node pacemaker activity. Circ Res. 2003;92:e41–e44.
6 Lancaster MK, Jones SA, Harrison SM, Boyett MR. Intracellular Ca^{2+} and pacemaking within the rabbit sinoatrial node: heterogeneity of role and control. J Physiol. 2004;556(Pt 2):481–494.
7 Melnyk P, Ehrlich JR, Pourrier M, Villeneuve L, Cha TJ, Nattel S. Comparison of ion channel distribution and expression in cardiomyocytes of canine pulmonary veins versus left atrium. Cardiovasc Res. 2005;65:104–116.
8 Tanaka H, Shigenobu K. Species difference in myocardial excitation-contraction coupling featuring the mouse. Curr Topics Pharmacol. 2003;7:247–256.
9 Tanaka H, Sekine T, Nishimaru K, Shigenobu K. Role of sarcoplasmic reticulum in myocardial contraction of neonatal and adult mice. Comp Biochem Physiol A Mol Integr Physiol. 1998;120:431–438.
10 Kurokawa J, Suzuki T, Furukawa T. New aspects for the treatment of cardiac diseases based on the diversity of functional controls on cardiac muscles: Acute effects of female hormones on cardiac ion channels and cardiac repolarization. J Pharmacol Sci. 2009;109:334–340.
11 Sugiyama A, Ishida Y, Satoh Y, Aoki S, Hori M, Akie Y, et al. Electrophysiological, anatomical and histological remodeling of the heart to AV block enhances susceptibility to arrhythmogenic effects of QT-prolonging drugs. Jpn J Pharmacol. 2002;88:341–350.
12 Takahara A, Nakamura H, Nouchi H, Tamura T, Tanaka T, Shimada H, et al. Analysis of arrhythmogenic profile in a canine model of chronic atrioventricular block by comparing in vitro effects of the class III antiarrhythmic drug nifekalant on the ventricular action potential indices between normal heart and atrioventricular block heart. J Pharmacol Sci. 2007;103:181–188.
13 Kato Y, Masumiya H, Agata N, Tanaka H, Shigenobu K. Developmental changes in action potential and membrane currents in fetal, neonatal and adult guinea-pig ventricular myocytes. J Mol Cell Cardiol. 1996;28:1515–1522.
14 Agata N, Tanaka H, Shigenobu K. Developmental changes in action potential properties of the guinea pig myocardium. Acta Physiol Scand. 1994;149:331.
15 Nouchi H, Kiryu N, Tanaka H, Shigenobu K. Developmental changes in the effect of K channel blockers on the chick ventricular action potential. J Pharmacol Sci. 2007;103:SuppI I:202P.
16 Tanaka H, Sekine T, Kawanishi T, Nakamura R, Shigenobu K. Intrasarcomere $[Ca^{2+}]$ gradients and their spatio-temporal relation to Ca^{2+} sparks in rat cardiomyocytes. J Physiol. 1998;508:145–152.
17 Seki S, Nagashima M, Yamada Y, Tsutsuura M, Kobayashi T, Namiki A, et al. Fetal and postnatal development of Ca^{2+} transients and Ca^{2+} sparks in rat cardiomyocytes. Cardiovasc Res. 2003;58:535–548.
18 Tanaka H, Masumiya H, Sekine T, Kawanishi T, Hayakawa T, Miyata S, et al. Involvement of Ca^{2+} waves in excitation contraction coupling of rat atrial cardiomyocytes. Life Sci. 2001;70:715–726.
19 Endoh M. Signal transduction and Ca^{2+} signaling in intact myocardium. J Pharmacol Sci. 2006;100:525–537.
20 Ishii K, Shigenobu K. Kasuya Y. Postjunctional supersensitivity in young rat heart produced by immunological and chemical sympathectomy. J Pharmacol Exp Ther. 1982;220:209–215.
21 Ishii K, Ishii N, Shigenobu K, Kasuya Y. Acetylcholine supersensitivity in the rat heart produced by neonatal sympathectomy. Can J Physiol Pharmacol. 1985;63:898–899.
22 Tanaka H, Shigenobu K. Role of β-adrenoceptor-adenylate cyclase system in the developmental decrease in sensitivity to isoproterenol in fetal and neonatal rat heart. Br J Pharmacol. 1990;100:138–142.
23 Tanaka H, Kasuya Y, Shigenobu K. Altered responsiveness to autonomic transmitters of hearts from neonatal spontaneously hypertensive rats. J Cardiovasc Pharmacol. 1988;12:678–682.
24 Ieda M, Fukuda K. New aspects for the treatment of cardiac diseases based on the diversity of functional controls on cardiac muscles: The regulatory mechanisms of cardiac innervation and their critical roles in cardiac performance. J Pharmacol Sci. 2009;109:348–353.
25 Okumura S, Suzuki S, Ishikawa Y. New aspects for the treatment of cardiac diseases based on the diversity of functional controls on cardiac muscles: Effects of targeted disruption of the type 5

adenylyl cyclase gene. J Pharmacol Sci. 2009;109:354–359.
26 Tanaka H, Manita S, Matsuda T, Adachi M, Shigenobu K. Sustained negative inotropism mediated by alpha-adrenoceptors in adult mouse myocardia: developmental conversion from positive response in the neonate. Br J Pharmacol. 1995;114:673–677.
27 Tanaka H, Namekata I, Takeda K, Shimizu Y, Moriwaki R, Hirayama W, et al. Unique excitation -contraction characteristics of mouse myocardium as revealed by SEA0400, a specific inhibitor of Na^+-Ca^{2+} exchanger. Naunyn Schmiedebergs Arch Pharmacol. 2005;371:526–534.
28 Nishimaru K, Tanaka Y, Tanaka H, Shigenobu K. α-Adrenoceptor stimulation-mediated negative inotropism and enhancement of Na^+-Ca^{2+} exchange in mouse ventricle. Am J Physiol. 2001; 280:H132–H141.
29 Sekine T, Kusano H, Nishimaru K, Tanaka Y, Tanaka H, Shigenobu K. Developmental conversion of inotropism by endothelin I and angiotensin II from positive to negative in mice. Eur J Pharmacol. 1999;374:411–415.
30 Nouchi H, Kaeriyama S, Muramatsu A, Sato M, Hirose K, Shimizu N, et al. Muscarinic receptor subtypes mediating positive and negative inotropy in the developing chick ventricle. J Pharmacol Sci. 2007;103:75–82.
31 Nishimaru K, Tanaka Y, Tanaka H, Shigenobu K. Positive and negative inotropic effects of muscarinic receptor stimulation in mouse left atria. Life Sci. 2000;66:607–615.
32 Tanaka H, Nishimaru K, Kobayashi M, Matsuda T, Tanaka Y, Shigenobu K. Acetylcholine-induced positive inotropism mediated by prostaglandin released from endocardial endothelium in mouse left atrium. Naunyn Schmiedebergs Arch Pharmacol. 2001;363:577–582.
33 Gover GJ, Sleph PG. Dissociation of cardiodepression from cardioprotection with calcium antagonists: diltiazem protects ischemic rat myocardium with a lower functional cost as compared with verapamil or nifedipine. J Cardiovasc Pharmacol. 1989;14:331–340.
34 Tanaka H, Matsui S, Kawanishi T, Shigenobu K. Use of chloride blockers: a novel approach for cardioprotection against ischemia-reperfusion damage. J Pharmacol Exp Ther. 1996;278: 854–861.
35 Namekata I, Nakamura H, Tanaka H, Shigenobu K. Cardioprotection without cardiosuppression by SEA0400, a novel inhibitor of Na^+-Ca^{2+} exchanger, during ischemia-reperfusion injury in guinea-pig myocardium. Life Sci. 2005;77:312–324.
36 Namekata I, Shimada H, Kawanishi T, Tanaka H, Shigenobu K. Reduction by SEA0400 of myocardial ischemia-induced cytoplasmic and mitochondrial Ca^{2+} overload. Eur J Pharmacol. 2006;533:108–115.
37 Nishida H, Sato T, Ogura T, Nakaya H. New aspects for the treatment of cardiac diseases based on the diversity of functional controls on cardiac muscles: Mitochondrial ion channels and cardioprotection. J Pharmacol Sci. 2009;109:341–347.
38 Sanbandam N, Lopaschuk GD, Brownsey RW, Allard MF. Energy metabolism in the hypertrophied heart. Heart Failure Rev. 2002;7:161–173.
39 Agata N, Kato Y, Tanaka H, Shigenobu K. Differential effects of hypoxia on electrical and mechanical activities of isolated ventricular muscles from fetal and adult guinea pigs. Gen Pharmacol. 1994;25:15–18.

Division of Drugs[1], National Institute of Health Sciences; Bruker Optics K.K.[2], Tokyo; TDDS Laboratory[3], Hisamitsu Pharmaceutical Co Inc, Ibaraki; Tokyo Metropolitan Industrial Technology Research Institute[4], Tokyo, Japan

Chemical mapping of tulobuterol in transdermal tapes using Microscopic Laser Raman Spectroscopy

T. Sakamoto[1], T. Matsubara[2], D. Sasakura[2], Y. Takada[3], Y. Fujimaki[4], K. Aida[3], T. Miura[2], T. Terahara[3], N. Higo[3], T. Kawanishi[1], Y. Hiyama[1]

Received July 29, 2008, accepted August 5, 2008

Tomoaki Sakamoto, Ph.D., National Institute of Health Sciences, 1-18-1, Kami-yoga, Setagaya-ku, Tokyo 158-8501, Japan
tsakamot@nihs.go.jp

Pharmazie 64: 166–171 (2009) *doi: 10.1691/ph.2008.8217*

Microscopic Laser Raman Spectroscopy and Mapping (MLRSM) technique was used to investigate the distribution of tulobuterol (TBR) crystals in transdermal tapes. TBR is one of suitable compounds for the transdermal pharmaceuticals because it has high permeability into skin. In case of TBR transdermal tapes, some commercial products also contain TBR crystals in order to control a release rate from a matrix. Therefore, the presence of TBR crystals in the matrix is a critical factor for quality assurance of this type of TDDS tapes. The model tapes prepared here employed two kinds of matrices, i.e., rubber or acrylic, which are generally used for transdermal pharmaceuticals. TBR crystals in the matrix were observed by MLRSM. Accurate observation of the distribution of TBR in the tapes was achieved by creating a Raman chemical map based on detecting unique TBR peak in each pixel. Moreover, differences in the growth of TBR crystals in the two kinds of matrices were detected by microscopic observation. MLRSM also enabled the detection of TBR crystals in commercial products. The present findings suggest that Raman micro-spectroscopic analysis would be very useful for verifying and/or assessing the quality of transdermal pharmaceuticals in development, as well as for manufacturing process control.

1. Introduction

Tulobuterol (TBR) transdermal tapes are applied in cases of bronchial asthma as a bronchodilator (β_2-blocker). TBR suitable for use in transdermal drug delivery because it has high permeability into the keratin layer (Uematsu et al. 1993). TBR pharmaceutical products with a Transdermal Drug Delivery System (TDDS) have advantages such as eliminating the side effects including abdominal pain and appetite loss (Iikura et al. 1995), and maintaining effective blood TBR levels for approximately 24 h (Horiguchi et al. 2004). The release rate of TBR from the matrix is controlled by the formation of TBR crystals. The crystallization of TBR has the possibility of influencing the TBR blood level profile. Therefore, it is necessary to characterize not only the release rate of TBR from a matrix, but also to characterize its crystallinity in dosage form in the matrix. *In vitro* penetration testing using stripped animal skin and *in vitro* release testing have been used to evaluate transdermal pharmaceuticals in terms of penetration and release. Because these evaluation methods show only one of several alternative physicochemical parameters (e.g., release rate, rate of penetration rate of an active substance, etc.), it has remained difficult to clarify the chemical status and quality of transdermal pharmaceuticals. In case of transdermal tapes containing an active drug as crystals in a matrix, the active drug is slowly released from the matrix into the keratin layer, as crystals will gradually dissolve in a matrix. Therefore, the crystallization of TBR is an important quality parameter. However, evaluation of the correlation of release rates between animal skin and human skin using *in vitro* penetration testing of animal skin has also remained difficult. Therefore, it has become desirable to develop analytical methods of both microscopically and chemically detecting and observing crystals of active drugs in a matrix.

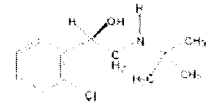

Tulobuterol (TBR)

Laser Raman spectroscopy is a method of spectroscopic analysis of spectra of Raman scattered light obtained by exposure of a sample to a laser. Raman spectroscopy has been used for the identification and quantification of polymorphs (Deely et al. 1991; Falcon et al. 2004; Ferrari et al. 2004; Findlay et al. 1998; Hu et al. 2005; Langkilde et al. 1997; Ono et al. 2004; Schöll et al. 2006; Starbuck et al. 2002; Wang et al. 2000; Murphy et al. 2005) and for monitoring the crystallization process (Taylor et al. 1998;

Murphy et al. 2005; Nørgaard et al. 2005) because it enables the detection of crystals, and in particular, differences between crystal forms. Therefore, Microscopic Laser Raman Spectroscopy/Mapping (MLRSM) was employed in the present study to microscopically and chemically detect TBR crystals in transdermal tapes. The applicability of this spectroscopic analytical method was examined both for the purpose of quality control (i.e., to confirm the crystals of TBR in the matrix), as well as with the aim of enhancing our understanding of relevant quality attributes of prototype pharmaceuticals in various stages of development.

2. Investigations and results

2.1. Determination of a unique wave number range in the Raman spectrum for TBR in model tapes

A typical Raman spectrum obtained from the TBR reference standard substance is shown in Fig. 1. Typical spectra of placebo tape (a) and model tape (b) of rubber matrices are shown in Figs. 2 and 3, respectively. To find characteristic wave numbers of TBR, these spectra were compared with the Raman spectrum obtained from a model tape. The peak bending vibration of C–C at 415cm^{-1} was used as the characteristic peak of TBR, and the integrated values obtained from the wave number range from 420 cm^{-1} to 400 cm^{-1} were used for making the Raman chemical maps.

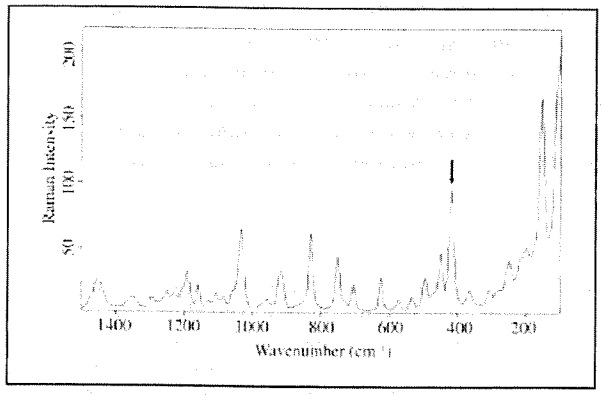

Fig. 1: Typical Raman spectrum of the TBR reference standard. The peak at 415 cm^{-1} was chosen as characteristic, because no interfering peak was observed in the vicinity of this peak

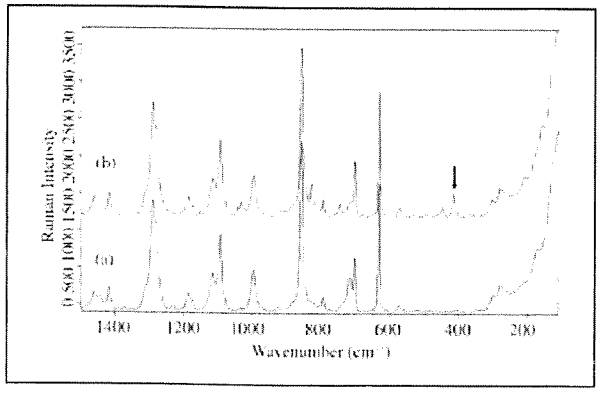

Fig. 2: Typical Raman spectra of placebo (a, rubber matrix) and model tape (b, rubber matrix). The arrow indicates the peak chosen for the specific detection of TBR. Comparatively strong intensity was observed

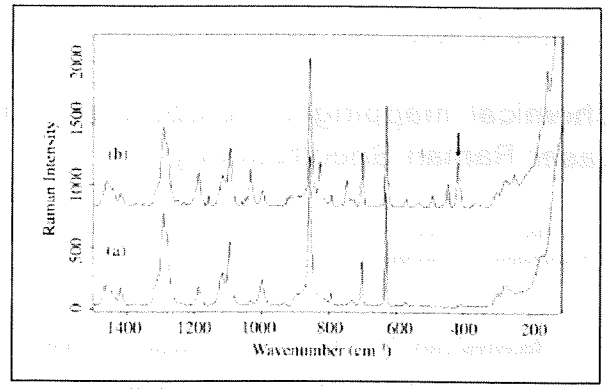

Fig. 3: Typical Raman spectra of placebo (a, acrylic matrix) and model tape (b, acrylic matrix). The very similar Raman spectrum of placebo tape was observed compared with that of the rubber matrix, because the absorption of supporting boards that were made from PET was also detected

2.2. Optical micrograph and Raman chemical mapping of the crystals of TBR in a rubber matrix

Figure 4a shows the micrograph of a 600 × 500 µm area in the R-10 sample. An enlarged micrograph (200 × 200 µm) is shown in Fig. 4b. Pillar-shaped crystals (short, 1 µm–2 µm; long, 10 µm–20 µm) that formed in lumps were observed. Figure 4c and d show the three-dimensional (3D) map and the Raman chemical map that corresponds with the area in Fig. 4b. In the Raman chemical map, the distribution of TBR in the matrix corresponded with the distribution of crystals in the optical micrograph. The Raman absorbance intensity corresponded with the distribution of optically observed TBR.

2.3. Optical micrograph and Raman chemical mapping of the crystals of TBR in an acrylic matrix

A micrograph of a 600 × 500 µm area and an enlarged micrograph of a 200 × 200 µm area of the A-20 sample are shown in Fig. 5a and b, respectively. In Figure 5c and d, the respective 3D chemical map and Raman chemical map are given that correspond to Fig. 5b. A lump of crystals with radiating branches was observed in the matrix. The Raman chemical map of TBR corresponding to the micrograph was obtained. The Raman chemical maps, which show the distribution of Raman chemical intensity, indicated trace amounts of crystal growth.

2.4. Shapes of crystals of TBR in two types of matrix

The micrograph of early-stage TBR crystallization in an acrylic matrix is shown in Fig. 6a. A lump of crystals with radiating branches was observed. Figure 6b shows the micrograph obtained approximately at the level of the top of branch of the crystal. The findings suggest that the pillar-shaped crystals were successively generated at the top of branches, and that the branches grew radially from the core. In case of the rubber matrix, pillar-shaped crystals that formed individual lumps were observed, as shown in Fig. 4a and b. No signs of a core were observed, and lumps of pillar-shaped crystals occurred individually in the matrix. These findings suggest that the TBR crystal growth mechanism differs in the two types of matrix analyzed here. Empirical evidence suggests that when crystallization was rapid, numerous crystalline lumps lacking a nucleus appeared in all areas of the ma-

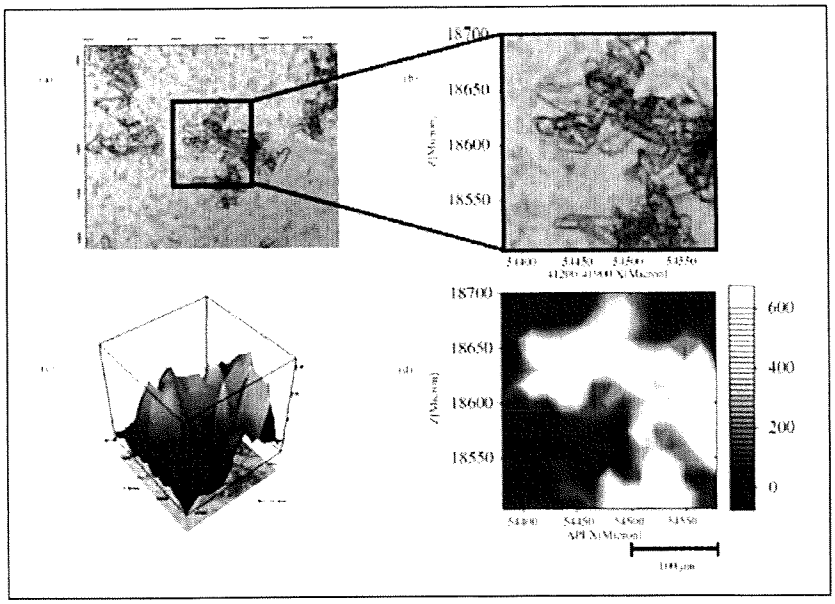

Fig. 4:
Micrographs and Raman chemical maps obtained from the model tape (R-10). a: Micrograph of a 600 × 500 μm area, b: Enlarged micrograph of a 200 × 200 μm area, c: 3D Raman chemical map that corresponds with that in d, d: Raman chemical map that corresponds with b. The distribution of the TBR crystals in the matrix was clearly detected by both methods

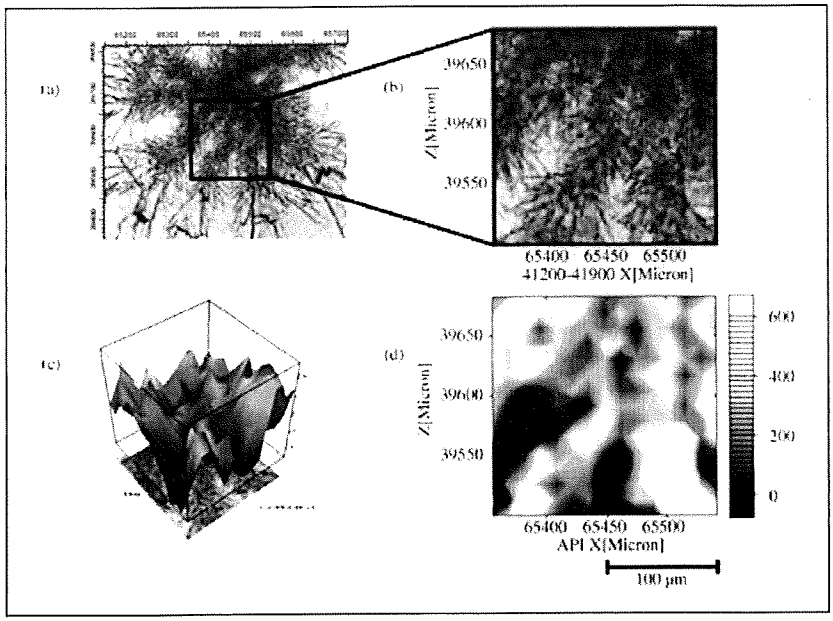

Fig. 5:
Micrographs and Raman chemical maps obtained from the model tape (A-20). a: Micrograph of a 600 × 500 μm area, b: Enlarged micrograph of a 200 × 200 μm area, c: 3D Raman chemical map that corresponds with d, d: Raman chemical map that corresponds with b. The mass of the crystals, with radiating branches, was observed in the matrix. The Raman chemical map of TBR corresponding to the micrograph was obtained

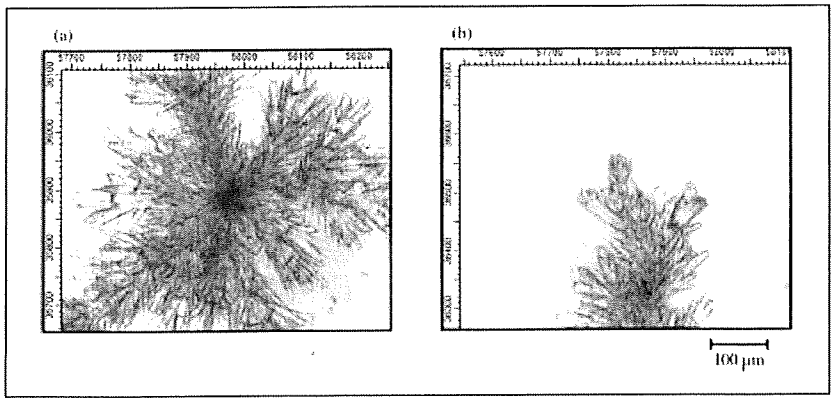

Fig. 6:
Micrographs of the mass of TBR crystals obtained from A-20. a: Core with radiating branches, b: Top of the branch. Pillar-shaped crystals generated successively at the top of branches were observed microscopically